Electronic structure of topological defects in the pair density wave superconductor

Marcus Rosales and Eduardo Fradkin

Department of Physics and Institute for Condensed Matter Theory, University of Illinois Urbana-Champaign, 1110 West Green Street, Urbana, Illinois 61801, USA

(Received 18 June 2024; revised 12 October 2024; accepted 16 October 2024; published 11 December 2024)

Pair density waves (PDWs) are a inhomogeneous superconducting states whose Cooper pairs possess a finite momentum resulting in a oscillatory gap in space, even in the absence of an external magnetic field. There is growing evidence for the existence of PDW superconducting order in many strongly correlated materials, particularly in the cuprate superconductors and in several other different types of systems. A feature of the PDW state is that inherently it has a CDW as a composite order associated with it. Here we study the structure of the electronic topological defects of the PDW, paying special attention to the half-vortex and its electronic structure that can be detected in STM experiments. We discuss tell-tale signatures of the defects in violations of inversion symmetry, in the excitation spectrum and their spectral functions in the presence of topological defects. We discuss the "Fermi surface" topology of Bogoliubov quasiparticle of the PDW phases, and we briefly discuss the role of quasiparticle interference.

DOI: 10.1103/PhysRevB.110.214508

I. INTRODUCTION

One of the central problems in condensed matter physics is understanding the phases of strongly correlated systems such as high-T_c superconductors. Experimental and theoretical research during the past decade has clearly shown that a characteristic feature of these systems is that their complex phase diagrams have phases with different types of charge, spin, and superconducting orders which are intertwined rather than competing with each other [1]. The prototype quantum materials with intertwined orders are the cuprate superconductors, which possess a very rich phase diagram hosting antiferromagnetic order, high-temperature d-wave superconductivity, CDW order, nematic order, and, at least in the lanthanum family of cuprates, incommensurate SDW order. Experiments done during the past decade have provided increasing evidence that, in addition to the d-wave superconducting order, in these systems a type of superconducting order, known as a pair density wave, may be at play [2]. In addition, and in contrast to conventional superconductors where the superconducting (SC) state is born from a normal Fermi liquid, the "normal" (high-temperature) state of all the cuprates is a strange metal, one without well-defined electronic quasiparticle.

Of particular interest is the cuprate material $La_{2-x}Ba_xCuO_2$ (LBCO). This cuprate superconductor, the original high-T_c material, has the interesting phase diagram provided in Fig. 1 [3]. Instead of a single SC dome, as most other cuprates have, $La_{2-x}Ba_xCuO_4$ has a pronounced anomaly at $x = 1/8$ hole doping where the transition temperature to the d-wave SC state is suppressed dramatically from 35 K to about 4 K where the Meissner state is observed. In this regime a remarkable set of phase transitions are observed [4]: static charge-density-wave (CDW) and spin-density-wave (SDW) orders onset at 52 K and 42 K, respectively. Below the onset of the SDW order the c-axis resistivity, ρ_c, increases with decreasing temperature while the ab-plane resistivity, ρ_{ab}, decreases rapidly. Superconducting phase fluctuations in the ab planes onset at about 35 K, and at approximately 16 K a two-dimensional Berezhinskii-Kosterlitz-Thouless (BKT) transition to a two-dimensional SC state is observed. On the other hand, the resistive transition where the c-axis resistivity vanishes happens only at 10 K, and the full Meissner d-wave SC state is reached only at $T_c \sim 4$ K. This "dynamical layer decoupling" behavior is also observed in $La_{2-x}Ba_xCuO_4$ in the presence of a c-axis magnetic field away from $x = 1/8$ [5] and in underdoped $La_{2-x}Sr_xCuO_4$ in magnetic fields $B \sim 8$ T [6] where a magnetic-field induced SDW was observed long ago [7]. Similar behaviors have been found in LSCO doped with Zn [8] and with iron [9].

The remarkable dynamical layer decoupling observed at the 1/8 anomaly of $La_{2-x}Ba_xCuO_4$ implies that the interlayer Josephson effect is suppressed in this regime. Berg and coworkers [10] proposed that that the complex behavior of $La_{2-x}Ba_xCuO_4$ at $x = 1/8$ was evidence for the presence of the pair density wave made evident by the lattice structure of the low-temperature-tetragonal (LTT) crystal phase of $La_{2-x}Ba_xCuO_4$ [11,12].

Evidence for PDW order also exists in cuprate superconductors that do not have the LTT crystal structure such as $Bi_2Sr_2CaCu_2O_{8+\delta}$. In this case much of the evidence was found in STM experiments [13] and Josephson tunneling spectroscopy [14]. STM experiments in the vortex halo of $Bi_2Sr_2CaCu_2O_{8+\delta}$ have revealed tell-tale evidence for PDW order in that regime [15,16]. Recent experiments have provided evidence for PDW order to be present also in the superconducting states of several strongly correlated materials including the heavy fermion material UTe_2 [17,18], the iron superconductor Fe(Se,Te) [19], the pnictide $EuRbFe_4As_4$ [20], and kagome superconductors such as CsV_3Sb_5 [21,22]. In this study we will focus on the pristine PDW with no uniform component present. In a future publication we will

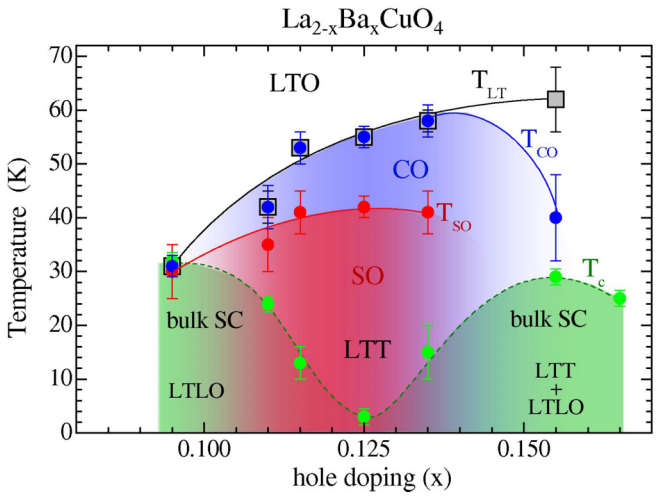

FIG. 1. Experimental data of LBCO indicating various phases for temperature, T, vs hole doping, x. Various orders exist simultaneously under the superconducting dome, which may indicate the onset of the PDW phase. Data from Ref. [3].

address how the uniform component affects various plots seen in this paper.

The PDW is a superconducting state in which Cooper pairs with finite center of mass momentum $\boldsymbol{Q}$ condense. In such a state the local pairing amplitude $\Delta(\boldsymbol{r})$ is periodic function of position whose period is $2\pi/|\boldsymbol{Q}|$. The order parameter of the PDW has the same symmetry as the Larkin-Ovchinnikov (LO) state [23]. However, the PDW differs from the LO state in several important ways: (1) the LO state is created by a magnetic field through the Zeeman coupling to the spins and it is spin-polarized and (2) as a result, it has a broken time-reversal invariance. In contrast, the PDW arises *in the absence of a magnetic field*. Another superconducting state with a finite-momentum Cooper pair is the Fulde-Ferrell (FF) state [24], which, like the LO state, was also envisioned as arising in the presence of a Zeeman coupling to an external magnetic field. Much like the LO state, the FF state breaks time reversal, but, in addition, it breaks inversion symmetry. The amplitude of the FF state is constant in space. Finally the ordering wave vectors of the LO and the FF states are tuned by the strength of the magnetic field, and, consequently, the periodicity of both states is much larger than the lattice constant.

In the cuprates, and in other candidate materials for PDW superconductors, the periodicity is a few lattice spacings. For all these reasons the "classic" FF and LO states are not suitable to explain the observed phenomenology of the cuprates and other materials. The phenomenology of the PDW state [2,10,25–27] (and the phenomenology of all high-temperature superconductors) strongly suggests that, with some possible exceptions, a PDW is necessarily a strong coupling state, which cannot be explained in terms of the conventional BCS theory of superconductivity [28,29]. Nevertheless, BCS-type approaches have been developed to explain the PDW [30–33] which require that the interactions be large compared to the kinetic energy of the holes. In this regime BCS theory is not reliable. Numerical simulations of $t-J$ and extended Hubbard models have shown evidence that PDW ground is at least a strong competitor to be ground state [34–38]. Quasi-one-dimensional models have also shown that their phase diagrams contain PDW phases [39]. Under special circumstances weak coupling models do predict the existence of PDW phases, but typically they require some other strong coupling physics to take place first, such as a Pomeranchuk instability in the triplet channel [40]. We should note that a recent study [41] predicts the occurrence of a PDW state in transition metal dichalcogenide materials. To the best of our knowledge the only microscopic model which is unambiguously known to have a (large) PDW phase is the one-dimensional Kondo-Heisenberg chain [42,43].

The purpose of this paper is to investigate physics of the PDW state by studying the electronic structure of the topological defects of this state: the half-vortex, the double dislocation, and the Abrikosov vortex. The study that we undertake here is relevant to the understanding of the features of these defects revealed by STM experiments. Here we adopt a phenomenological description of the PDW, and we will not concern ourselves with the possible physical mechanism(s) associated with this superconducting state. For concreteness we will consider a system with a square lattice (kagome and honeycomb lattices have also been considered). On a square lattice the PDW state may be unidirectional, which breaks spontaneously both translation symmetry and the point group symmetry of the square lattice, or bidirectional, which is invariant under the point group symmetry but breaks translation symmetry along two directions. Let $\Delta(\boldsymbol{r})$ be the local amplitude for a spin singlet superconductor (where $\boldsymbol{r}$ is a lattice site; in the case of a local d-wave state $\boldsymbol{r}$ is the superconducting amplitude on a bond between two nearest-neighbor sites $\boldsymbol{r}$ and $\boldsymbol{r}'$). We will consider the simpler case of an unidirectional spin-singlet PDW with a period close to $8a_0$, which is appropriate for the lanthanum cuprates [2]. The local pairing amplitude can be expanded in Fourier components

$$\Delta(\boldsymbol{r}) = \Delta_0(\boldsymbol{r}) + \Delta_{\boldsymbol{Q}}(\boldsymbol{r})e^{i\boldsymbol{Q}\cdot\boldsymbol{r}} + \Delta_{-\boldsymbol{Q}}(\boldsymbol{r})e^{-i\boldsymbol{Q}\cdot\boldsymbol{r}}, \tag{1.1}$$

where $\Delta_0(\boldsymbol{r})$ is the uniform component. Here we denoted by $\Delta_{\pm\boldsymbol{Q}}(\boldsymbol{r})$ the two PDW components with wave vectors $\pm\boldsymbol{Q}$. We will not include higher harmonics in the order parameter occurring at $n\mathbf{Q}$ since in the ordered state these orders are slaved to the fundamental and hence are not independent dynamical degrees of freedom [44].

The PDW equilibrium state is a phase in which the uniform component vanishes, $\langle\Delta_0\rangle = 0$, and the two Fourier components have the same expectation value, $\langle\Delta_{\boldsymbol{Q}}\rangle = \langle\Delta_{-\boldsymbol{Q}}\rangle = \Delta_{\rm PDW}$. If $\langle\Delta_0\rangle \neq 0$ and $\Delta_{\rm PDW} \neq 0$ the resulting state is a striped superconductor. Most proposed PDW states (outside the lanthanum cuprates) are actually striped superconductors. Finally, in the FF state $\langle\Delta_{\boldsymbol{Q}}\rangle$ or (exclusive) $\langle\Delta_{-\boldsymbol{Q}}\rangle$ are not zero.

In this paper we will consider only a unidirectional PDW state and hence assume that $\langle\Delta_0\rangle = 0$. The central results of this paper are concerned with experimental signatures associated with the induced CDW "daughter" states of the PDW parent state [25,45]. The induced CDW order with wave vector $\boldsymbol{K} = 2\boldsymbol{Q}$ whose order parameter field is $\rho_{2\boldsymbol{Q}}(\boldsymbol{r}) \sim \Delta_{\boldsymbol{Q}}\Delta^*_{-\boldsymbol{Q}}$ [and similarly for $\rho_{-2\boldsymbol{Q}}(\boldsymbol{r})$] is described in more detail in Sec. II, including the topological defects of the PDW state we are interested in. The unidirectional PDW has

two complex order parameters, $\Delta_{\pm \boldsymbol{Q}}(\boldsymbol{r})$, which means two amplitude fields and two phase fields. This means that the order parameter of the PDW transforms under a $U(1) \times U(1)$ global symmetry, where the first factor is the conventional global $U(1)$ gauge invariance of a superconductor, and the second factor represents the invariance under continuous translations of the *incommensurate* PDW state. In Refs. [25,45] it is shown that as a result of the topology of the target space of the order parameter(s) of the PDW, this state has three distinct topological defects: a superconducting Abrikosov vortex, a half-vortex, and a double dislocation.

The electronic structure of the PDW has Bogoliubov quasiparticle with (Bogoliubov) Fermi surfaces, which define pockets of quasiparticle states [25,46]. The stability of Bogoliubov Fermi surfaces has been established in several studies [47,48]. In the PDW state the half-vortex has an energy cost which diverges logarithmically with sample size. In contrast, in the presence of a nonvanishing uniform SC component, $\langle \Delta_0 \rangle \neq 0$, the energy cost is instead *linearly divergent* and, hence, half-vortices and anti-half-vortices are *confined* into pairs. Experimental evidence for half-vortices pairs has been found in STM experiments in $Bi_2Sr_2CaCu_2O_{8+\delta}$ by Du and coworkers [14].

In this work we describe the half-vortex as a state in which one of the two order parameters of the PDW, say, $\Delta_{\boldsymbol{Q}}(\boldsymbol{r})$, has a vortex while the other order parameter, $\Delta_{-\boldsymbol{Q}}(\boldsymbol{r})$, does not. Since *one* of the SC order parameters vanishes at the defect location while the other does not, at the defect core we have an FF-type state which breaks inversion symmetry. In this sense, the half-vortex has an FF halo. This behavior is analogous to the halo associated with the Abrikosov vortex in a system in which uniform SC and PDW orders compete [15,16]. Our construction of the half-vortex follows the same strategy used by Wang and coworkers [16] for the Abrikosov vortex halo of an uniform superconductor with a PDW as a subleading order. In contrast, in the case of a Abrikosov vortex *both* PDW order parameters wind with the same topological charge, whereas in the double dislocation they wind with opposite topological charges.

We then investigate the electronic structure of the PDW in the presence of topological defects by embedding the resulting configuration into the Bogoliubov–de Gennes Hamiltonian. Here we use a noninteracting band structure suitable for a superconductor in a copper oxide plane. Using this effective Hamiltonian with the defect background we calculated the local density of states and a function of bias for a model of an STM measurement at a point contact with a normal metal. We also compare the results on the half-vortex with the same calculation done for a full Abrikosov vortex and for a double dislocation of the CDW.

The paper is organized as follows. In Sec. II we introduce the Landau-Ginzburg equations to be used in our analysis. In this section the notion of intertwined order is reviewed, and we discuss the composite order parameters of interest in Sec. II B. An overview of the relationship between experiment and induced order is briefly discussed there as well. In Sec. II C we review the topological defects of the PDW superconducting state. Section III is devoted to the construction of a static half-vortex. Here we discuss how the profiles of the components of the PDW order parameters are modeled in the case of a half-vortex. In Sec. IV the effective mean field Hamiltonian for the PDW with static topological defects used in our simulation is introduced as well as the Green functions and the related spectral function. Here we present results for the local density of states (LDOS), used to acquire plots for the numerical solutions. In Sec. IV the numerical parameters and the explicit form of the order parameters used in the simulation are discussed. In Sec. IV B the plots of the charge-density-wave order of the PDW in the presence of defects are shown, and various other aspects of the vortex cores are explored and discussed. In Sec. IV E we discuss the spectral functions of the PDW order and display the dispersion relation for a PDW with a half-vortex. Finally, in Sec. V we discuss some implications of our results and summarize the most salient results. Several Appendixes are devoted to technical details. Details of the Bogoliubov transformation are given in Appendix A, and the setup for the numerical diagonalization of the Bogoliubov–de Gennes Hamiltonian is sketched in Appendix B. In Appendix C we give details of the retarded Green function at zero temperature. In Appendix E we compare the tunneling DOS for a PDW, an FF state, and the half-vortex of the PDW. In Appendix F we present data on spectral functions for PDW states with s- and d-wave form factors.

II. LANDAU-GINZBURG THEORY

In this section we review the Landau-Ginzburg (LG) theory for a unidirectional PDW state [25], which will be used to describe the profiles of our order parameters in the presence of static topological defects. In a a later section we will calculate the local density of states (LDOS) in the presence of topological defects that we will describe in this section. Because our defects are static, we will be neglecting fluctuations, so our analysis here will be done at the level of mean field theory. Furthermore, we also work deep in the PDW phase where the order parameters have well-defined local amplitudes, which is justified at low temperatures.

A. Free energy of the PDW state

The free energy of the LG theory is chosen to have the form

$$\mathcal{F}[\Delta_0, \Delta_{\mathbf{Q}}, \Delta_{-\mathbf{Q}}] = \mathcal{F}_{\rm sc}[\Delta_0] + \mathcal{F}_{\rm pdw}[\Delta_{\mathbf{Q}}, \Delta_{-\mathbf{Q}}]. \tag{2.1}$$

The first term in Eq. (2.1) describes uniform superconductivity, which takes the familiar form

$$\mathcal{F}_{\rm sc} = \frac{1}{2m^*}|(-i\nabla + 2e\mathbf{A})\Delta_0|^2 + \frac{a}{2}|\Delta_0|^2 + \frac{b}{2}|\Delta_0|^4. \tag{2.2}$$

In this paper our main results correspond to a defect-free PDW in the absence of an uniform component: $\Delta_0 = 0$. We will mention the effects of a nonzero uniform component when relevant, but in the majority of this paper we neglect it. Furthermore, we will assume that the PDW is unidirectional, characterized by a single ordering wave vector $\boldsymbol{Q}$. We will also ignore the effects of disorder. This is important since, unlike a conventional uniform superconductor, a PDW can couple to local charge disorder through the interaction of the induced CDW associated with the PDW. In fact, in the presence of disorder the distinction between unidirectional and bidirectional orders is lost as these PDW components get mixed with each other [49].

The second term in Eq. (2.1) describes the free energy of the unidirectional PDW. In Eq. (1.1) we presented the expansion of the local pairing amplitude $\Delta(\boldsymbol{r})$ in its Fourier components $\Delta_{\pm\boldsymbol{Q}}(\boldsymbol{r})$, where $\Delta_{\pm\boldsymbol{Q}}(\boldsymbol{r})$ are the order parameters of the unidirectional PDW state with ordering wave vector $\boldsymbol{Q}$. Since the local pairing amplitude $\Delta(\boldsymbol{r})$ is a complex field, the two PDW components $\Delta_{\pm\boldsymbol{Q}}$ are not the complex conjugate of each other (as they would have been for a CDW) but are two independent complex fields. The PDW free energy has the form [1,25,26,45]

$$\begin{aligned}\mathcal{F}_{\rm pdw}[\Delta_{\mathbf{Q}},\Delta_{-\mathbf{Q}}]&=\kappa(|\nabla\Delta_{\mathbf{Q}}|^2+|\nabla\Delta_{-\mathbf{Q}}|^2)+r(|\Delta_{\mathbf{Q}}|^2+|\Delta_{-\mathbf{Q}}|^2)\\&\quad+u(|\Delta_{\mathbf{Q}}|^2+|\Delta_{-\mathbf{Q}}|^2)^2+\gamma|\Delta_{\boldsymbol{Q}}|^2|\Delta_{-\boldsymbol{Q}}|^2,\end{aligned}\tag{2.3}$$

where $r=T-T_c^{\rm pdw}$, and $T_c^{\rm pdw}$ is the (mean-field) critical temperature for the PDW superconductor. We will assume that the coupling constant $\gamma<0$ as needed for an attractive interaction needed for a PDW, an LO-type state. Instead, a repulsive value of the coupling constant, $\gamma>0$, favors an FF-type state.

The PDW state is described by two independent *complex* order parameters fields $\Delta_{\pm\boldsymbol{Q}}(\boldsymbol{r})$. Since they are complex fields they can be decomposed into amplitude and phase fields, $\Delta_{\pm\boldsymbol{Q}}(\boldsymbol{r})=|\Delta_{\pm\boldsymbol{Q}}(\boldsymbol{r})|\exp[i\theta_{\pm\boldsymbol{Q}}(\boldsymbol{r})]$, respectively. For general values of the coupling constants u and γ the free energy for the PDW order parameters, Eq. (2.3), is invariant under the $U(1)\times U(1)$ global symmetries $\theta_{\pm\boldsymbol{Q}}(\boldsymbol{r})\to\theta_{\pm\boldsymbol{Q}}(\boldsymbol{r})+\vartheta_{\pm\boldsymbol{Q}}$, where $\vartheta_{\pm\boldsymbol{Q}}$ are two independent transformations of the phases of the complex fields $\Delta_{\pm\boldsymbol{Q}}(\boldsymbol{r})$. In the special case in which $\gamma=0$ this global symmetry is enhanced from $U(1)\times U(1)$ to $U(2)$.

In many superconductors of interest, such as cuprates $Bi_2Sr_2CaCu_2O_{8+\delta}$ and $La_{2-x}Ba_xCuO_4$ in the Meissner state, a uniform superconducting order parameter Δ_0 is present. This results in the following additional "lock-in" terms that couple the three superconducting order parameters, and it must be added to the free energy of Eq. (2.1):

$$\mathcal{F}_I=\beta_1|\Delta_0|^2(|\Delta_{\boldsymbol{Q}}|^2+|\Delta_{-\boldsymbol{Q}}|^2)+\beta_2(\Delta_0^*)^2\Delta_{\boldsymbol{Q}}\Delta_{-\boldsymbol{Q}}+\text{c.c.}\tag{2.4}$$

The first term is the usual biquadratic term which is attractive (repulsive) for $\alpha<0$ ($\alpha>0$). The second term breaks the $U(1)\times U(1)$ global symmetry down to the global $U(1)$ symmetry of the uniform superconductor and locks (mod π) the phase fields of the PDW order parameters $\Delta_{\pm\boldsymbol{Q}}(\boldsymbol{r})$ to the phase field of the uniform superconducting order parameter $\Delta_0(\boldsymbol{r})\equiv|\Delta_0(\boldsymbol{r})|\exp[i\theta_0(\boldsymbol{r})]$, which transforms under global gauge transformations in the usual way, $\theta_0(\boldsymbol{r})\to\theta_0(\boldsymbol{r})+\vartheta_0$.

B. Order parameters of the PDW state

With the above SC orders we can construct the following set of composite order parameters [25,26]:

$$\rho_{\boldsymbol{Q}}(\boldsymbol{r})=\Delta_0(\boldsymbol{r})\Delta_{\boldsymbol{Q}}^*(\boldsymbol{r}),\tag{2.5}$$

$$\rho_{2\boldsymbol{Q}}(\boldsymbol{r})=\Delta_{\boldsymbol{Q}}(\boldsymbol{r})\Delta_{-\boldsymbol{Q}}^*(\boldsymbol{r}),\tag{2.6}$$

$$\Delta_{4e}(\boldsymbol{r})=\Delta_{\mathbf{Q}}(\boldsymbol{r})\Delta_{-\mathbf{Q}}(\boldsymbol{r}).\tag{2.7}$$

The two order parameters of Eqs. (2.5) and (2.6) are interpreted as the $\boldsymbol{Q}$ and $2\boldsymbol{Q}$ components of a CDW associated with the PDW SC order. The order parameter of Eq. (2.7) represents an uniform charge $4e$ superconductor.

Following the analysis of Berg *et al.* [25] we decompose the phase fields of the PDW order parameters as

$$\theta_{\pm\boldsymbol{Q}}(\boldsymbol{r})=\theta_+(\boldsymbol{r})\pm\theta_-(\boldsymbol{r}).\tag{2.8}$$

Under the global $U(1)\times U(1)$ gauge transformations defined above the order parameters transform as follows:

$$\Delta_{\pm\boldsymbol{Q}}(\boldsymbol{r})\to\exp[i(\vartheta_+\pm\vartheta_-)]\Delta_{\pm\boldsymbol{Q}}(\boldsymbol{r}),\tag{2.9}$$

$$\Delta_0(\boldsymbol{r})\to\exp(i\vartheta_0)\Delta_0(\boldsymbol{r}),\tag{2.10}$$

$$\rho_{\boldsymbol{Q}}(\boldsymbol{r})\to\exp[i(\vartheta_0-\vartheta_+)]\exp(i\vartheta_-)\rho_{\boldsymbol{Q}}(\boldsymbol{r}),\tag{2.11}$$

$$\rho_{2\boldsymbol{Q}}(\boldsymbol{r})\to\exp(i2\vartheta_-)\rho_{2\boldsymbol{Q}}(\boldsymbol{r}),\tag{2.12}$$

$$\Delta_{4e}(\boldsymbol{r})\to\exp(i2\vartheta_+)\Delta_{4e}(\boldsymbol{r}),\tag{2.13}$$

where we defined the global gauge transformations $\vartheta_\pm=(\vartheta_{\boldsymbol{Q}}\pm\vartheta_{-\boldsymbol{Q}})/2$.

Under a global *electromagnetic* gauge transformation all three superconducting order parameters must transform as charge $2e$ complex fields and, consequently, $\vartheta_0=\vartheta_+$. With this identification the CDW order parameter $\rho_{\boldsymbol{Q}}$ is manifestly invariant under global gauge transformations. Similarly, the order parameter Δ_{4e} transforms under global gauge transformations as a charge $4e$ field.

On the other hand, the composite order parameter field $\rho_{\pm2\boldsymbol{Q}}(\boldsymbol{r})$ has the same transformation as that of the order parameter for an *incommensurate* CDW under an arbitrary global *translation*. The slowly varying relative phase of the two PDW order parameters is identified with the Goldstone mode of the spontaneously broken translation invariance of the PDW state. In an incommensurate (unidirectional) CDW state with wave vector $\boldsymbol{K}$, the local charge density $\rho(\boldsymbol{r})$ has the Fourier expansion

$$\rho(\boldsymbol{r})=\bar\rho+\rho_{\boldsymbol{K}}(\boldsymbol{r})\exp(i\boldsymbol{K}\cdot\boldsymbol{r})+\rho_{-\boldsymbol{K}}(\boldsymbol{r})\exp(-i\boldsymbol{K}\cdot\boldsymbol{r})+\cdots,\tag{2.14}$$

where $\rho_{\boldsymbol{K}}=\rho_{-\boldsymbol{K}}^*$ since $\rho(\boldsymbol{r})$ is real and invariant under global gauge transformation, and where the ellipsis denotes higher harmonics of the density wave. Thus, the PDW has an associated charge density modulation with wave vector $\boldsymbol{K}=2\boldsymbol{Q}$ [10]. An arbitrary relative phase transformation by θ (mod 2π) is then equivalent to a displacement of the charge density profile by $2\theta/|\boldsymbol{K}|$. In the case of a CDW which is commensurate with the underlying lattice with period p lattice spacings, pa_0, the CDW wave vector is $|\boldsymbol{K}|=2\pi/pa_0$. In this case the allowed transformations of the relative phase take discrete p values. In this case the $U(1)$ symmetry group of translations reduces to the discrete (cyclic) group $\mathbb{Z}_p$. In this case the PDW is locked to the lattice, it has p equivalent ground states, and the Goldstone mode of translations is gapped.

Alternatively, the incommensurate CDW may be a present as a preexisting order with wave vector $\boldsymbol{K}$. Such a CDW cannot couple to an (also incommensurate) PDW unless the CDW ordering wave vector $\boldsymbol{K}$ and the PDW ordering wave vector $\boldsymbol{Q}$ satisfy the *mutual commensurabilty condition* $\boldsymbol{K}=2\boldsymbol{Q}$. This interaction is described by an additional trilinear term in the

free energy of the form

$$\mathcal{F}_{\text{PDW}-\text{CDW}} = g\,\rho_{\boldsymbol{K}}\Delta_{\boldsymbol{Q}}\Delta^*_{-\boldsymbol{Q}} + \text{c.c.}, \tag{2.15}$$

where g is a coupling constant [25]. Translation invariance then requires that the mutual commensurability condition is satisfied. The same requirement exists for a coupling between a spin density wave *SDW*. This effect is seen in $La_{2-x}Ba_xCuO_4$ at the charge-ordering transition [50] and in $La_{1.8-z}Eu_{0.2}Sr_xCuO_4$ [51] at low temperatures. The existence of this interaction yields some interesting physics not allowed for an uniform SC state: the PDW is sensitive to charged impurities due to their coupling to the CDW. Thus, unlike uniform superconducting order, which is weakened only by disorder, even small amounts of charge disorder destroy true long-range incommensurate PDW order.

C. Topological defects of the PDW state

We will now discuss the topological defects of the PDW phase. For now we will set $\Delta_0 = 0$, and we will be brief as many details exist in the literature [25,45]. The phase fields, which we denote by $\theta_{\pm\boldsymbol{Q}}(\boldsymbol{r})$, are periodic and defined mod 2π. Hence, the topological singularities of the phase fields $\theta_{\pm\boldsymbol{Q}}(\boldsymbol{r})$ have integer-valued winding numbers, $m_{\pm\boldsymbol{Q}}$. This implies that $\theta_\pm(\boldsymbol{r})$, the average and relative phase fields $\theta_\pm(\boldsymbol{r}) = (\theta_{\boldsymbol{Q}} \pm \theta_{-\boldsymbol{Q}})/2$ be defined mod π. We denote the topological charge of the average phase $\theta_+(\boldsymbol{r})$ by the vortex charge q_v and the topological charge of the relative $\theta_-(\boldsymbol{r})$, the dislocation topological charge of the CDW, by q_d. They are given by

$$q_v = \tfrac{1}{2}(m_{\boldsymbol{Q}} + m_{-\boldsymbol{Q}}), \quad q_d = \tfrac{1}{2}(m_{\boldsymbol{Q}} - m_{-\boldsymbol{Q}}). \tag{2.16}$$

We will label the topological defects by the combinations (q_v, q_d), the vorticity and dislocation charges, or equivalently, $(m_{\boldsymbol{Q}}, m_{-\boldsymbol{Q}})$. In the simplest cases they are (1) the *superconducting (Abrikosov) vortex* with topological charges $(q_v, q_d) = (\pm 1, 0)$ [or, equivalently, $(m_{\boldsymbol{Q}}, m_{-\boldsymbol{Q}}) = (\pm 1, \pm 1)$], (2) the *half-vortex* (bound to a single CDW dislocation) with topological charges $(q_v, q_d) = (\pm 1/2, \pm 1/2)$ [or, equivalently, $(m_{\boldsymbol{Q}}, m_{-\boldsymbol{Q}}) = (\pm 1, 0)$], and (3) the CDW *double dislocation* with topological charges $(q_v, q_d) = (0, \mp 1)$ [or, equivalently, $(m_{\boldsymbol{Q}}, m_{-\boldsymbol{Q}}) = (\pm 1, \mp 1)$]. These identifications imply that a conventional superconducting vortex is equivalent to *both* PDW order parameters $\Delta_{\pm\boldsymbol{Q}}$ having a vortex. The half-vortex is equivalent to a vortex in $\Delta_{\boldsymbol{Q}}$ but *not* in $\Delta_{-\boldsymbol{Q}}$ (and vice versa), and it has a single-dislocation, as required by Eq. (2.6). Finally, a double dislocation is a vortex in $\Delta_{\boldsymbol{Q}}$ and an antivortex in $\Delta_{-\boldsymbol{Q}}$ (and vice versa).

In the PDW state the energy of all three types of topological defects is logarithmically divergent, leading to the rich phase diagram of Ref. [25]. However, if the superconducting state also has a uniform component, $\Delta_0 \neq 0$, the lock-in term of Eq. (2.4) predicts a *linearly divergent* energy cost resulting in a confined neutral pair of half-vortices which cannot be excited thermally. In this case only the superconducting vortices and the double dislocations have logarithmic energy and govern the phase diagram.

In this paper we will focus primarily on the properties of the half-vortex, which we will regard as a *static* topological defect of an ordered PDW state which we will take to be of the Larkin-Ovchinnikov (LO) type [23]. Hence, we will assume that at long distances the PDW amplitudes are equal and constant in space, $|\Delta_{\boldsymbol{Q}}| = |\Delta_{-\boldsymbol{Q}}|$. However, at the core of the half-vortex one of these two amplitudes, say, $\Delta_{\boldsymbol{Q}}$, must vanish while the other amplitude does not. As a result, the core of the half-vortex is in a Fulde-Ferrell (FF) state [24], and inversion symmetry is broken at the core of the half-vortex since $|\Delta_{\boldsymbol{Q}}| \neq |\Delta_{-\boldsymbol{Q}}|$. On the other hand, none of these considerations apply to either the Abrikosov vortex or to the double dislocation.

As in all superconductors, the Abrikosov vortex of the PDW arises in the presence of a magnetic field. On the other hand, the half-vortex and the double dislocation can appear due to the interaction of the PDW state with sufficiently strong charged impurities. This is possible since the CDW order parameter $\rho_{2\boldsymbol{Q}}(\boldsymbol{r})$ of the PDW has a linear coupling to charged impurities potentials, whereas gauge invariance requires that the superconducting order parameters interact only quadratically through $|\Delta_{\pm\boldsymbol{Q}}(\boldsymbol{r})|^2$.

The properties of all three topological defects will be discussed in Sec. IV, where we specify the form of the order parameters used in the numerics. The associated charge density wave patterns of each defect will be compared in Sec. IV B as well as their spectral functions in Sec. IV E.

An extremely useful experimental technique for detecting and visualizing CDW patterns is scanning tunneling microscopy (STM) [52–55]. STM has been used to investigate in great detail the charge order present in the superconducting phase of $Bi_2Sr_2CaCu_2O_{8+\delta}$ [56–58] and in the vortex halo [15,16]. Relevant to the existence of PDW order is the experimental evidence for static (pinned) half-vortices in the superconducting phase of $Bi_2Sr_2CaCu_2O_{8+\delta}$ found in STM experiments by Du *et al.* [14]. These authors argued that the jumps in the PDW SC winding number are located around the charge dislocations. In this regime the term proportional to β_2 in Eq. (2.4) locks the phase of the PDW order parameter to the phase of the uniform superconducting state. The result is a confinement of the half-vortices into (half) vortex-antivortex pairs. Hence, in the phase in which the uniform order parameter is present, $\Delta_0 \neq 0$, the energy of the half-vortex is linearly divergent and half-vortices cannot exist in isolation. In this regime charged impurity potentials can separate the half-vortices and anti-half-vortices as static defects.

The basic setup for an STM consists of an atomically sharp metallic tip, with a featureless Fermi surface, biased at some voltage V relative to the sample. The voltage difference induces a tunneling current, $I_T(V)$, which is used to map out the electronic structure at the surface of a material. In the regime in which the STM operates, the differential conductance $g(V) = dI_T/dV$ is proportional to the one-particle density of states (DOS) $\rho(\epsilon = eV)$ at an energy $\epsilon = eV$.

III. THE HALF-VORTEX

In this section we will model the profile of our half-vortex of an unidirectional PDW, and we will assume that there is no uniform SC order. In Sec. IV we will embed the configuration of the half-vortex in a Bogoliubov–de Gennes Hamiltonian for the d-wave superconducting state of a CuO_2 plane and investigate its effects on the electronic structure. The Abrikosov

vortex and the double dislocation will also be considered in later sections, so we mention their solutions here as well. We should note that the associated CDW dislocation was given in Ref. [45].

We will seek an extremal solution of the Landau-Ginzburg free energy density $\mathcal{F}_{pdw}[\Delta_{\boldsymbol{Q}}(\boldsymbol{r}), \Delta_{-\boldsymbol{Q}}(\boldsymbol{r})]$ for the PDW order given in Eq. (2.3). In Sec. II we showed that a vortex with half magnetic flux quanta can be realized by putting a 2π phase winding in one of the two superconducting components $\Delta_{\pm\boldsymbol{Q}}$ of the unidirectional PDW order parameter. Thus, we will require the order parameter $\Delta_{\boldsymbol{Q}}(\boldsymbol{r})$ to have a unit vortex and set the other component to be real $\Delta_{-\boldsymbol{Q}}(\boldsymbol{r}) = |\Delta_{-\boldsymbol{Q}}(\boldsymbol{r})|$, and we set its phase $\theta_{-\boldsymbol{Q}} = 0$.

A half-vortex is an extremal solution of the PDW free energy $\mathcal{F}_{pdw}$ which at long distances behaves as a vortex in $\Delta_{\boldsymbol{Q}}$:

$$\lim_{|\boldsymbol{r}|\to\infty} \Delta_{\boldsymbol{Q}}(\boldsymbol{r}) = \Delta_{pdw}\, \exp(i\varphi),$$
$$\lim_{|\boldsymbol{r}|\to\infty} \Delta_{-\boldsymbol{Q}}(\boldsymbol{r}) = \Delta_{pdw}, \tag{3.1}$$

where $\tan\varphi = y/x$, where $\boldsymbol{r} = (x, y)$. Notice that we require the amplitude Δ_{pdw} asymptotically to be the same for both $\Delta_{\pm\boldsymbol{Q}}$ so that at long distances we have a PDW (LO) state.

On the other hand, since $\Delta_{\boldsymbol{Q}}$ has a vortex, its amplitude must vanish at the origin. Instead, $\Delta_{-\boldsymbol{Q}}$ does not have to vanish at the origin, and it will take some finite value, which we denote as Δ_{ff}. In other words, in the presence of a half-vortex the superconducting order has an FF component. Hence, at short distances the half-vortex must have the behavior

$$\lim_{|\boldsymbol{r}|\to 0} \Delta_{\boldsymbol{Q}}(\boldsymbol{r}) = 0,$$
$$\lim_{|\boldsymbol{r}|\to 0} \Delta_{-\boldsymbol{Q}}(\boldsymbol{r}) = \Delta_{ff}. \tag{3.2}$$

The precise profile of the configuration of the half-vortex depends on the parameters of the PDW free energy $\mathcal{F}_{pdw}$ of Eq. (2.3): the stiffness κ, the PDW critical temperature T_c^{pdw}, and the coupling constants u and $\gamma < 0$. The way the asymptotic values, Δ_{pdw} and Δ_{ff}, are attained depends on all the parameters of the free energy. There are two significant length scales (which also depend on these parameters): the scale over which the amplitude of $\Delta_{\boldsymbol{Q}}(\boldsymbol{r})$ decreases from Δ_{pdw} to zero (the "core" of the half-vortex), and the scale over which $\Delta_{-\boldsymbol{Q}}(\boldsymbol{r})$ interpolates between Δ_{pdw} and Δ_{ff} (the FF "halo" of the half-vortex).

In order to obtain an explicit expression for the field configuration of the half-vortex we will use a nonlinear sigma model approximation similar to the one used by Wang and coworkers in their study of the PDW halo of a superconducting vortex [16] (see also Ref. [59]). Thus, we define a three-component unit vector field $\boldsymbol{n}(\boldsymbol{r})$ such that

$$\boldsymbol{n}(\boldsymbol{r}) = \frac{1}{\Delta}\left(\mathrm{Re}\Delta_{\boldsymbol{Q}}(\boldsymbol{r}), \mathrm{Im}\Delta_{\boldsymbol{Q}}(\boldsymbol{r}), \Delta_{-\boldsymbol{Q}}(\boldsymbol{r})\right) \tag{3.3}$$

with $\boldsymbol{n}^2(\boldsymbol{r}) = 1$ everywhere, and where Δ will be determined below. Here we used that $\Delta_{-\boldsymbol{Q}}$ is a real field. With these assumptions the free energy density of the PDW, Eq. (2.3), becomes [with $\boldsymbol{n} = (n_x, n_y, n_z)$]

$$\mathcal{F}_{pdw} = \kappa\Delta^2(\nabla\boldsymbol{n})^2 + \left(T_c^{pdw} - T\right)\Delta^2 + u\Delta^4 - |\gamma|\Delta^4 n_z^2\left(n_x^2 + n_y^2\right). \tag{3.4}$$

We will set Δ to be the value $\bar{\Delta}$ that minimizes the free energy in the uniform PDW phase; that is, using

$$\boldsymbol{n}_{pdw} = \frac{1}{\sqrt{2}}(1, 0, 1) \tag{3.5}$$

we find

$$\bar{\Delta} = \sqrt{\frac{2\left(T_c^{pdw} - T\right)}{4u - |\gamma|}}. \tag{3.6}$$

The free energy density $\mathcal{F}_{nlsm}$ of the unit vector field $\boldsymbol{n}(\boldsymbol{r})$ becomes

$$\mathcal{F}_{nlsm} = \bar{\kappa}(\nabla\boldsymbol{n})^2 - v n_z^2\left(n_x^2 + n_y^2\right) + \text{const}, \tag{3.7}$$

where we used the definitions $\bar{\kappa} \equiv \kappa\bar{\Delta}^2$ and $v \equiv |\gamma|\bar{\Delta}^4$, with $\bar{\Delta}$ given in Eq. (3.6).

We will now construct the half-vortex of the PDW using the nonlinear sigma model (NLSM) of Eq. (3.7). We assume that the ordering wave vector of the PDW is oriented along the x axis and write $\mathbf{Q} \equiv Q\mathbf{e}_x$. We will also assume that the phase field $\varphi(\mathbf{r})$ winds by 2π, and we define its branch cut along the positive x axis. With these assumptions we define the unit vector

$$\mathbf{e}_{\mathbf{r}} = \cos[\varphi(\mathbf{r})]\mathbf{e}_x + \sin[\varphi(\mathbf{r})]\mathbf{e}_y, \tag{3.8}$$

and write the $O(3)$ NLSM field $\boldsymbol{n}(\boldsymbol{r})$ in the form

$$\mathbf{n}(\mathbf{r}) = \sin[\alpha(\mathbf{r})]\mathbf{e}_{\mathbf{r}} + \cos[\alpha(\mathbf{r})]\mathbf{e}_z. \tag{3.9}$$

In Sec. II we defined the half-vortex as a configuration in which the phase field of $\Delta_{\boldsymbol{Q}}$ winds by 2π at infinity while the order parameter field $\Delta_{-\boldsymbol{Q}}$ does not wind and is defined to be real. The order parameters of the PDW in the half-vortex state are required to obey the boundary conditions of Eq. (3.1) (at long distances) and Eq. (3.2) (at short distances). As a result, the half-vortex has an FF-type order within the core and asymptotically far from the core is of LO-type. Such a state breaks inversion symmetry in the core of the half-vortex. In terms of the NLSM field $\boldsymbol{n}(\boldsymbol{r})$ the boundary conditions of Eqs. (3.1) and (3.2) become

$$\lim_{r\to 0} \boldsymbol{n}(\mathbf{r}) = (0, 0, 1), \tag{3.10}$$
$$\lim_{r\to\infty} \boldsymbol{n}(\boldsymbol{r}) = \frac{1}{\sqrt{2}}(\cos\varphi(\boldsymbol{r}), \sin\varphi(\boldsymbol{r}), 1), \tag{3.11}$$

where, as before, we defined the phase $\varphi(\boldsymbol{r})$, to be the azimuthal angle measured from the positive x axis, with $\tan\varphi(\boldsymbol{r}) = y/x$, which winds by 2π on a large circle. To satisfy these boundary conditions we will require the field $\alpha(\boldsymbol{r})$ to be isotropic, $\alpha(\boldsymbol{r}) \equiv \alpha(r)$, and to satisfy the boundary conditions

$$\lim_{r\to 0} \alpha(r) = 0, \quad \lim_{r\to\infty} \alpha(r) = \pi/4. \tag{3.12}$$

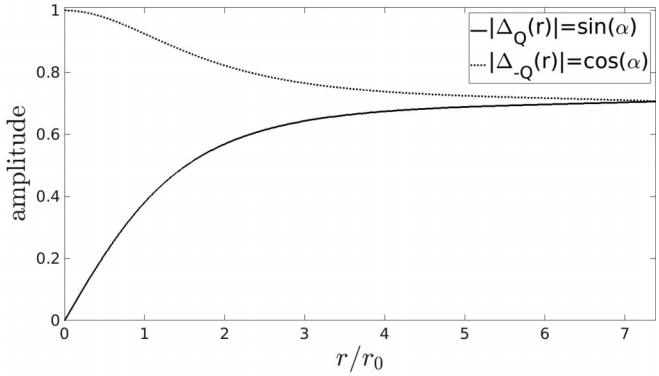

FIG. 2. Plots of the profiles for the two components of the PDW order parameters, $|\Delta_{\pm \boldsymbol{Q}}(r)|$, measured in units of $\bar{\Delta}$ given in Eq. (3.6). We define the vortex radius to be the place where $|\Delta_{-\boldsymbol{Q}}|$ has an inflection point; in this plot this is at $r/r_0 = 1$.

After performing some algebra, we can recast the total free energy of the NLSM, Eq. (3.7), into the following form:

$$F[\mathbf{n}] = 2\pi\bar{\kappa}\int rdr\left[\left(\frac{\partial\alpha}{\partial r}\right)^2 + \frac{\sin^2(\alpha)}{r^2} - \frac{v}{\bar{\kappa}}\sin^2(\alpha)\cos^2(\alpha)\right] \tag{3.13}$$

$$= 2\pi\bar{\kappa}\int dt\left[\left(\frac{\partial\alpha}{\partial t}\right)^2 + \sin^2(\alpha) - e^{2t}\sin^2(\alpha)\cos^2(\alpha)\right], \tag{3.14}$$

where in line we defined $r_0^2 = \bar{\kappa}/v$ and made the change of variables $t = \ln(r/r_0)$, where $t \in (-\infty, \infty)$, for $r \in [0, \infty)$. In our numerics the half-vortex radius will be set to to be $r_0/a_0 = 8n$ where a_0 is the lattice spacing and n is an integer, which we vary. Upon extremizing the free energy $F(\boldsymbol{n})$ of Eq. (3.14) we find that $\alpha(t)$ must obey the "equation of motion":

$$\frac{d^2\alpha}{dt^2} = \frac{1}{2}[1 - \cos[2\alpha(t)]e^{2t}]\sin[2\alpha(t)] \tag{3.15}$$

such that the boundary conditions of Eq. (3.12) now become

$$\lim_{t\to-\infty}\alpha(t) = 0, \quad \lim_{t\to\infty}\alpha(t) = \pi/4. \tag{3.16}$$

A numerical solution of the equation of motion (3.15) yields the optimal solution for the half-vortex. Plots of the magnitudes of the PDW components (in units of $\bar{\Delta}$) as a function of distance from the vortex core are provided in Fig. 2(a). As is clear from this figure, as the amplitude $\Delta_{\boldsymbol{Q}}(r)$ *decreases* as $r \to 0$, the amplitude of $\Delta_{-\boldsymbol{Q}}(r)$ *increases* as $r \to 0$. In other words, the core of the half-vortex behaves as a FF state which breaks inversion symmetry. The parameter r_0 can be used to define the radius of the half-vortex. and it is set at the inflection of the $\Delta_{-\boldsymbol{Q}}(\mathbf{r})$ field (at $r/r_0 = 1$ in Fig. 2), which is related to the coherence length of the Cooper pairs. We can then see that the degree of inversion symmetry breaking depends on the area of the core of the half-vortex. In the absence of the uniform component Δ_0 the branch cut of the half-vortex is unobservable, resulting in a free energy that is only logarithmically divergent. However, if $\Delta_0 \neq 0$ the branch cut becomes observable and behaves as a *domain wall*. In this case the energy of the half-vortex becomes linearly divergent.

The profiles of the Abrikosov vortex and the double dislocation are obtained using a similar approach. In the cases of these topological defects both components of the PDW order parameter fields $\Delta_{\pm\boldsymbol{Q}}(\boldsymbol{r})$ have vorticity. In the case of the Abrikosov vortex we consider solutions of the Landau-Ginzburg equations with the the same vorticity and set $\Delta_{-\boldsymbol{Q}}(\mathbf{r}) = \Delta_{\boldsymbol{Q}}(\mathbf{r}) \equiv \Delta(\boldsymbol{r})$, where $\Delta(\boldsymbol{r})$ is a conventional Abrikosov vortex. Instead, in the case of the double dislocation we consider solutions in which the two PDW order parameters have equal and opposite vorticity, $\Delta_{\boldsymbol{Q}}(\boldsymbol{r}) = \Delta(\boldsymbol{r})$ and $\Delta_{-\boldsymbol{Q}}(\mathbf{r}) = \Delta^*(\mathbf{r})$, where again $\Delta(\boldsymbol{r})$ is a conventional vortex solution. The vortex solution has the form

$$\Delta(\boldsymbol{r}) = \bar{\Delta} f(r/r_0)\exp[i\varphi(\boldsymbol{r})], \tag{3.17}$$

where r_0 is the radius of the vortex and $\varphi(\boldsymbol{r})$ is the azimuthal angle on the plane. The profile function $f(r/r_0)$ is calculated numerically and satisfies the boundary conditions $\lim_{r\to0} f(r/r_0) = 0$ and $\lim_{r\to\infty} f(r/r_0) = 1$.

IV. PDW BOGOLIUBOV–de GENNES HAMILTONIAN WITH TOPOLOGICAL DEFECTS

In this section we describe the Bogoliubov–de Gennes Hamiltonian on the square lattice with a cuprate electronic structure with the configurations of the PDW order parameter in the background of the topological defects introduced in Secs. II and III. We will focus on the effects on the electronic states.

In order to study the effects of the different topological defects of the PDW state in the associated CDW order and in the electronic structure we consider a model which couples our electronic degrees of freedom to the local amplitude of the superconducting order parameter in the background of each defect, denoted by the pair field $\Delta(\boldsymbol{r}, \boldsymbol{r}')$ in the bonds $(\boldsymbol{r}, \boldsymbol{r}')$ of the square lattice. In what follows we will define $\Delta(\mathbf{r}, \mathbf{r}')$ as the embedding to the square lattice of the solutions of the Landau-Ginzburg equations for the pair field of a PDW in the background of the different topological defects.

We consider four configurations of the PDW order parameter, (1) the uniform PDW state, (2) the half-vortex, (3) the Abrikosov vortex, and (4) the double dislocation. Defined relative to the origin of the $\boldsymbol{r}$ plane, the configurations of the PDW order parameter take the following generic form:

$$\Delta_i(\mathbf{r}, \mathbf{r}') = \bar{\Delta}\, F(\mathbf{r}, \mathbf{r}')f_i(\mathbf{r}). \tag{4.1}$$

Here $\bar{\Delta}$ is the amplitude of the SC gap given in Eq. (3.6), $F(\mathbf{r}, \mathbf{r}')$ is the SC form factor, and $f_i(\mathbf{r})$ are the profiles and winding numbers of the four configurations of the PDW order parameters listed above. On a square lattice the form factor $F(\boldsymbol{r}, \boldsymbol{r}') = 1$ for an s-wave SC state. In a d-wave SC state, which is our focus, the form factor is $F(\boldsymbol{r}, \boldsymbol{r}') = 1(-1)$ for a bond $(\boldsymbol{r}, \boldsymbol{r}')$ on the x axis (y axis) of the square lattice and changes sign under a $\pi/2$ rotation. Using the results of Sec. III the explicit forms of the functions $f_i(\mathbf{r})$'s are

$$f_1(\mathbf{r}) = \cos(\mathbf{Q}\cdot\mathbf{r}),$$

$$f_2(\mathbf{r}) = \tfrac{1}{2}\{\sin[\alpha(\mathbf{r})]e^{i\mathbf{Q}\cdot\mathbf{r}+i\varphi(\mathbf{r})} + \cos(\alpha(\mathbf{r}))e^{-i\mathbf{Q}\cdot\mathbf{r}}\},$$

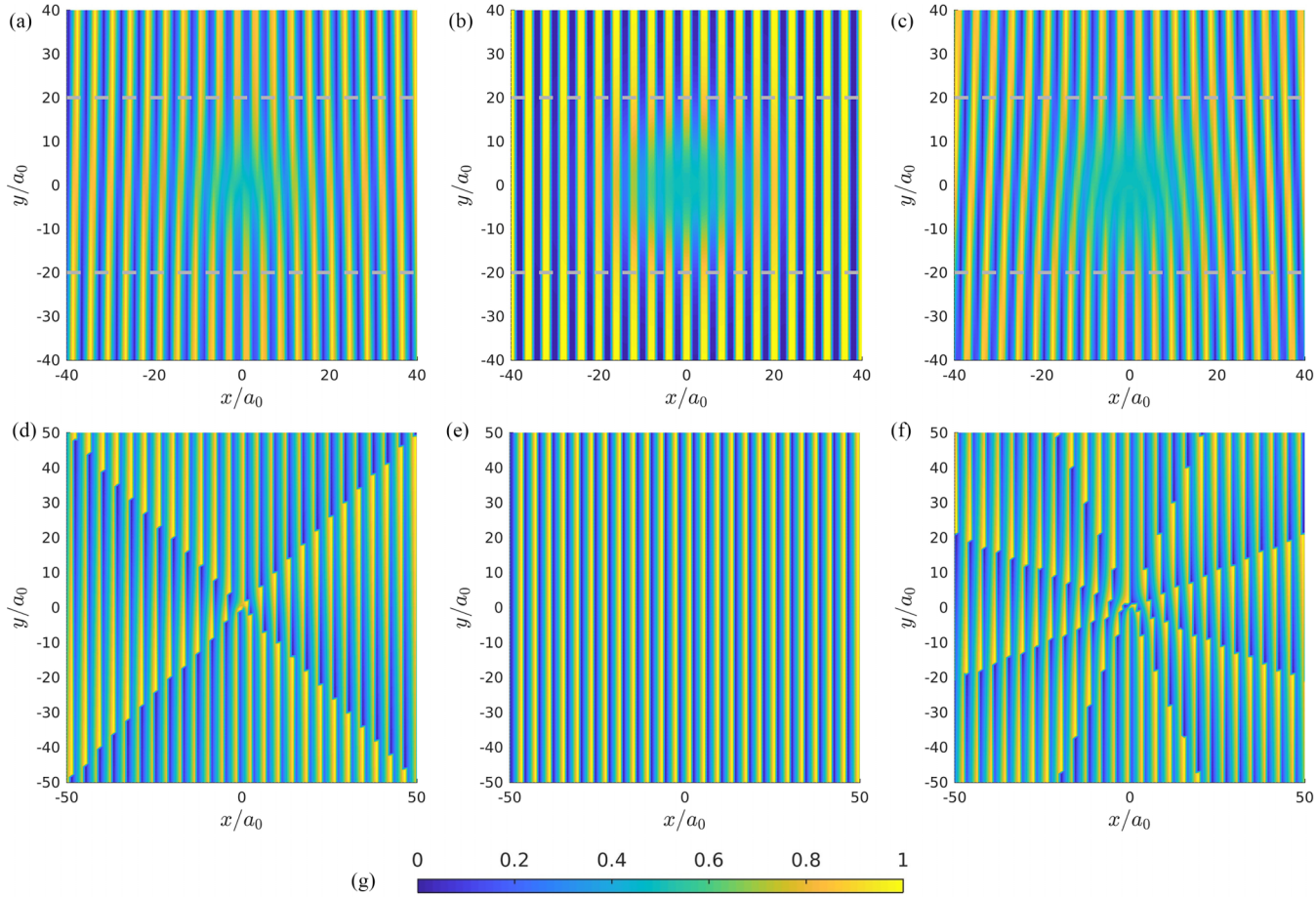

FIG. 3. Plots of the real parts of the daughter CDWs $\rho_{2\mathbf{Q}}(\mathbf{r})$ given by Eq. (2.6) defined in terms of the functions given in Eq. (4.2). Here the three topological defects have a vortex radius of $r_0 = 16a_0$ being (a) the half-vortex, (b) the Abrikosov vortex, and (c) the double dislocation. The dotted lines shown in light gray are guides to count the CDW peaks to find the associated Burgers vectors, being the difference of the top line and the bottom, As expected, in (a) for the half-vortex (which has a single dislocation) they skip by one, in (b) for the Abrikosov vortex they do not skip, and in (c) for the double dislocation they skip by two. In the second row, plots (d)–(f), we include the corresponding $\arg(\rho_{2\mathbf{Q}})$ for (d) the half-vortex, (e) the Abrikosov vortex, and (f) the double dislocation. The jumps in phase seen in these panels are $\pi/2$, and they sum up to the expected dislocation charge associated with a given defect. The color bar provided in (g) pertains to all plots. For (a)–(c) it corresponds to the scale of the defect (that is, we normalized these plots), and for (d)–(f) it represents units of 2π.

$$f_3(\mathbf{r}) = f(r/r_0)\cos(\mathbf{Q}\cdot\mathbf{r})e^{i\varphi(\mathbf{r})},$$
$$f_4(\mathbf{r}) = f(r/r_0)\cos[\mathbf{Q}\cdot\mathbf{r}+\varphi(\mathbf{r})]. \tag{4.2}$$

Here $\alpha(\mathbf{r})$ is the angle we used to parametrize the NLSM in Eq. (3.9), whose numerical solution was found in Sec. III. The vortex profile function $f(r/r_0)$ is defined in Eq. (3.17). Finally, the complex phase, $\varphi(\mathbf{r})$, is the azimuthal angle on the plane, and it winds by 2π in all the expressions in which it appears. In Figs. 3(a)–3(c) we show the profile of the composite order parameters $\rho_{2\mathbf{Q}}(\mathbf{r})$ (that is, we take the real part of this expression) in the presence of the three topological defects of our PDW order. The Burgers vector associated with a given charge dislocation can be found by simply counting the difference in the CDW peaks found above and below the vortex cores. The dotted lines are guides used to indicate where to do the counting. The profiles of the associated CDW order in the presence of the defects are shown in Sec. IV B. We also include $\arg(\rho_{2\mathbf{Q}})$ in Figs. 3(d)–3(f). Notice the four jumps in phase by $\pi/2$ for the half-vortex [Fig. 3(d)] and the eight jumps for the double dislocation [Fig. 3(f)], while there are none for the full vortex [Fig. 3(e)], reflecting the expected amount of dislocation charge present in each defect.

A. Hamiltonian and observables

The Bogoliubov–de Gennes (BdG) Hamiltonian for the lattice model is

$$\hat{H}_i = -\sum_{\mathbf{r},\mathbf{r}',\sigma} t(\mathbf{r}-\mathbf{r}')\hat{c}^\dagger_{\mathbf{r}\sigma}\hat{c}_{\mathbf{r}'\sigma} + \sum_{\mathbf{r},\mathbf{r}'}(\Delta_i(\mathbf{r},\mathbf{r}')\hat{c}^\dagger_{\mathbf{r}\uparrow}\hat{c}^\dagger_{\mathbf{r}'\downarrow} + \text{H.c.}) \tag{4.3}$$

for each configuration of the SC amplitudes $\Delta_i(\boldsymbol{r},\boldsymbol{r}')$ [see Eqs. (4.1) and (4.2)]. The normal state band structure we will be using is parameterized with values of hopping amplitudes of a tight-binding model on the square lattice chosen to best fit Angle-Resolved Photoemission Spectroscopy (ARPES) experiments in the high-temperature superconductors $La_{2-x}Ba_xCuO_4$ and $Bi_2Sr_2CaCu_2O_{8+\delta}$ [60,61]. The explicit parameters used (in units of eV) are $t = 0.25$, $t' =$

-0.031863, $t'' = 0.016487$, $t''' = 0.0076112$, and $\mu = -0.16235$. We also take the superconducting amplitude $\bar{\Delta} = 60$ meV. In all cases we assumed that the superconducting order parameter $\Delta(\boldsymbol{r}, \boldsymbol{r}')$ is a unidirectional PDW along the x direction with period eight lattice spacings, with a wave vector $\boldsymbol{Q} = (\pi/4, 0)$ (in units with $a = 1$).

Since the Fermi surface of the cuprates is not spherically symmetric, the PDW states along the nodal and antinodal directions have different features. The same applies for a putative FF state. Below we will show the Bogoliubov spectrum in the core of the half-vortex resembles that of a pristine FF state trapped inside. A wave vector oriented along the antinodal direction results in a fully gapped FF state, whereas for a state oriented in the nodal direction the resulting spectrum has nodes. In the situation of interest the FF state in the core of the half-vortex of the PDW is gapped.

The details of the diagonalization procedure can be found in Appendixes A and B. In short, we define a Nambu spinor, $\psi_+^T = [\mathbf{c}_\uparrow, \mathbf{c}_\downarrow^\dagger]$, which helps us perform the exact diagonalization (see Appendix B). These define our quasiparticle operators, $\hat{b}_l$ and $\hat{b}_l^\dagger$, which annihilate the BCS ground state and create single-particle excitations with energy E_l, respectively [62].

As in the case of a uniform superconductor, the excited states are an admixture of electrons and holes. We find our electron creation/annihilation operators are related to linear combinations of our quasiparticle operators: $\hat{c}_{i\sigma} = v_{il}^* \hat{b}_l^\dagger + \sigma u_{il} \hat{b}_l$. Here repeated indices are summed over, and the coefficients are the real space coherence factors.

In order to compare the spectroscopic properties of our system obtained from the states of the BdG Hamiltonian to experiment we use the zero temperature retarded Green functions and their Fourier transforms (see Appendix C). We will focus on two quantities of experimental interest, the LDOS $L(\boldsymbol{r}, \omega)$ and the spectral function $A(\boldsymbol{k}, \omega)$. In Appendix C we show that these quantities are given by

$$L(\mathbf{r}_i, \omega) = -\frac{1}{\pi}\mathrm{Im}(G(\mathbf{r}_i, \mathbf{r}_i, \omega)) = \frac{1}{\pi}\sum_{E_l \geqslant 0}\left(\frac{\epsilon}{(\omega - E_l)^2 + \epsilon^2}|u_{il}|^2 + \frac{\epsilon}{(\omega + E_l)^2 + \epsilon^2}|v_{il}|^2\right) \tag{4.4}$$

and

$$A(\mathbf{k}, \omega) = -\frac{1}{\pi}\mathrm{Im}(G(\mathbf{k}, \mathbf{k}, \omega)) = \frac{1}{\pi}\sum_{E_l \geqslant 0}\epsilon\left(\frac{|\tilde{u}_l(\mathbf{k})|^2}{(\omega - E_l)^2 + \epsilon^2} + \frac{|\tilde{v}_l(\mathbf{k})|^2}{(\omega + E_l)^2 + \epsilon^2}\right), \tag{4.5}$$

where $\tilde{u}_l(\boldsymbol{k})$ and $\tilde{v}_l(\boldsymbol{k})$ are the eigenvectors of the BdG equations in momentum space and the energy resolution will be taken to be $\epsilon = 2.5$ meV. Our simulations were also conducted on a 400×400 lattice to achieve the desired resolution for our spectral functions and Fourier transforms of the LDOS. We leave the consideration of the anomalous Green functions and its relations to Cooper pair tunneling for a future study.

B. Electronic structure of the PDW topological defects

In this subsection we analyze our numerical results for the LDOS, computed using Eq. (4.4), for the configurations of the PDW order parameter with the three topological defects defined in Eq. (4.2). The intertwining of the PDW defects with the induced CDW order will be discussed in detail, as well as the structure of the charge distribution induced by these defects. The main focus will be on experimental signatures associated with the CDW pattern induced by the half-vortex and the double dislocation. The superconducting properties of the PDW half-vortex will be discussed in Sec. IV D.

In Fig. 3 we plot the profiles of (i.e., we take the real part of) the resulting CDW order parameter $\rho_{2\boldsymbol{Q}}$ near the three topological defects given in Eq. (4.2) using the definition of Eq. (2.6). We note that in our numerics we take the form factor $F(\mathbf{r}, \mathbf{r}')$ to be defect-free d wave. Since the PDW order breaks the point group symmetry of the lattice, the form factor associated with the unidirectional PDW phase should be an admixture of s wave and d wave [16]. However, as was discussed in [63], there are robust features which are essentially the same for both form factors. In Appendix F, Fig. 14, we present the spectral functions for an order parameters with an s-wave form factor, but our primary focus will be on d-wave SC.

In Fig. 4 we show the changes in the LDOS of a the PDW state with the three topological defects whose CDW order parameter $\rho_{2\boldsymbol{Q}}$ near the defects are shown in Fig. 3. The LDOS of these defects are shown in Figs. 4(a)–4(c) for a probing voltage of $0.25\Delta_0$. These were obtained by computing numerically the tunneling density of states of the electronic states obtained from the BdG equations for the three defects. These patterns exhibit a sinusoidal PDW oscillatory component of four lattice spacings, as expected for a CDW with ordering wave vector $\boldsymbol{Q}_{cdw} = 2\boldsymbol{Q}$ [see Eq. (2.6)], superposed with various effects arising from the changes induced by the topological defects on the eigenstates of the BdG equation.

The charge density profiles associated with each of these defects reveals some of the most salient signatures of the PDW order. First and foremost, Fig. 4(a) shows the half-vortex, which can indeed be thought of as a dislocation in the CDW order parameter $\rho_{2\boldsymbol{Q}}(\boldsymbol{r})$ pinned to a half-SC-flux-quanta. The predicted forms of the other two topological defects have been discussed in the literature [2,44,45]. The double dislocation is shown in Fig. 4(c). As was the case for Fig. 3, the Burgers vector associated with these charge dislocations can be found by simply counting the difference in the CDW peaks found above and below the vortex cores. The full vortex has no dislocation charge [Fig. 4(b)]. Notice, however, the phase of background density wave pattern of the full vortex is shifted

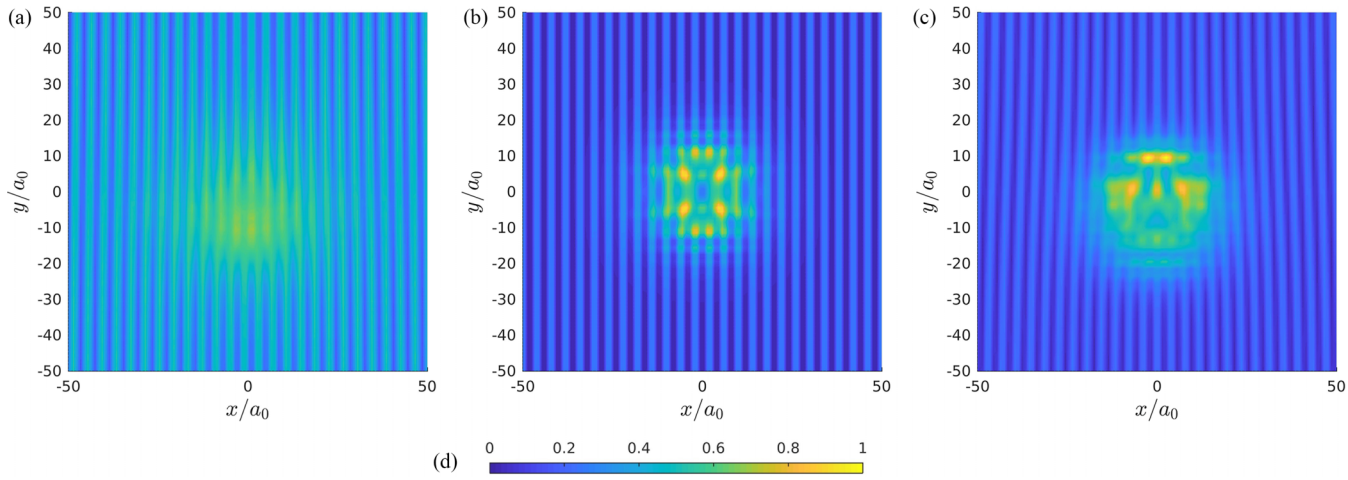

FIG. 4. The LDOS profiles of a PDW in the presence of the three topological defects given in Eq. (4.2). Using the states of the BdG Hamiltonian [Eq. (4.3)] the LDOS evaluated at $\omega = 0.25\ \bar{\Delta}$ for (a) the half-vortex, (b) the Abrikosov vortex, and (c) the double dislocation. In (d) we provide a normalized color bar for each of the plots. Note that each specific defect is rescaled according to their own maximum value, so that the vortex core shows up clearer.

by π relative to the pattern of the other two defects, which can easily be seen at $x/a_0 = 0$.

In Fig. 5 we plot the integrated LDOS (i.e., the static charge density) for all three defects to a voltage of $1.25\,\bar{\Delta}$, well above the PDW SC gap. A comparison of these plots with Fig. 3 shows, as expected, that the integrated LDOS yields the CDW pattern (for details of this approach see Ref. [55]). As expected, in both figures the CDW order parameter is suppressed in the core of the defects where one or both components of the PDW order parameters $\Delta_{\pm \boldsymbol{Q}}$ are suppressed.

Next we notice the additional patterns seen within the core of the defects in Figs. 4(b) and 4(c), the Abrikosov vortex and the double dislocation. *Both* PDW order parameters $\Delta_{\pm \boldsymbol{Q}}$ vanish in the core of the double dislocation and of the Abrikosov vortex; hence, the additional electronic structure residing in their cores, revealed by the LDOS, is due to quasiparticle states. Although the quasiparticle states are responsible for the additional LDOS, they are not bound to the core of these two types of topological defects. The PDW has pockets of quasiparticle and quasiholes in momentum space. This interpretation is confirmed by a computation of the Fourier transforms in momentum space of the LDOS at different energies for the Abrikosov vortex. Figure 13 in Appendix D shows the quasiparticle spectrum in the presence of the vortex, which confirms that these are propagating states and are not bound to the core of the defect. Thus this structure in the LDOS has to be interpreted as due to quasiparticle interference (QPI) at the defects.

On the other hand, the half-vortex in Fig. 4(a) does not posses the QPI patterns seen for the double dislocation and the Abrikosov vortex. This is because in the case of the half-vortex one component of the PDW is always nonzero, which results in a gap for the states within the half-vortex core where the PDW becomes effectively a fully gapped FF state. In contrast, in the cases of the Abrikosov vortex and of the double

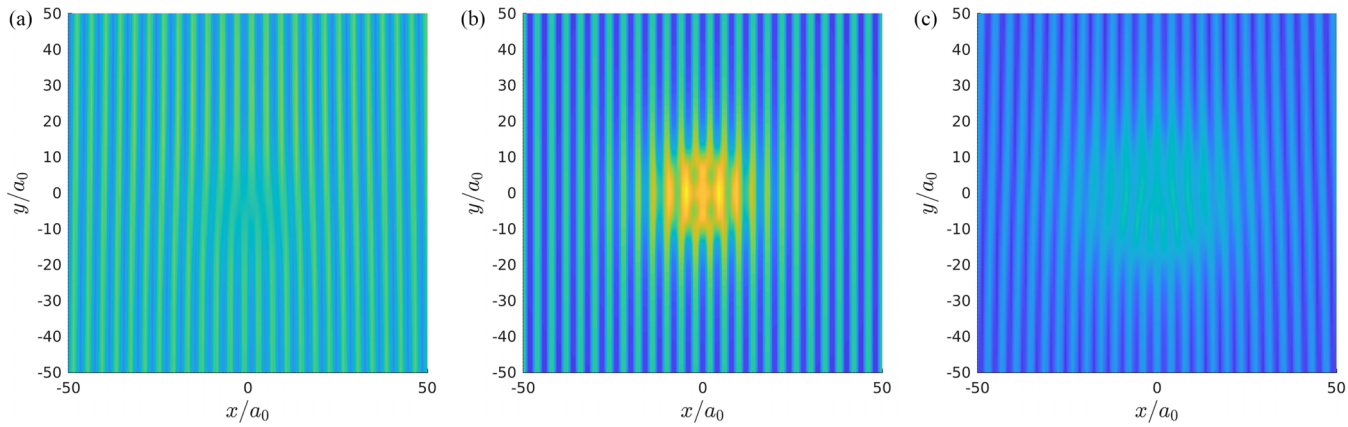

FIG. 5. Static charge density profiles obtained by integrating the LDOS out to a voltage of $1.25\,\bar{\Delta}$ in the presence of the three topological defects given in Eq. (4.2). Using the states of the BdG Hamiltonian [Eq. (4.3)] the LDOS for a PDW defects for (a) the half-vortex, (b) the Abrikosov vortex, and (c) the double dislocation. We take a scale normalized to the specific defect for each of these plots.

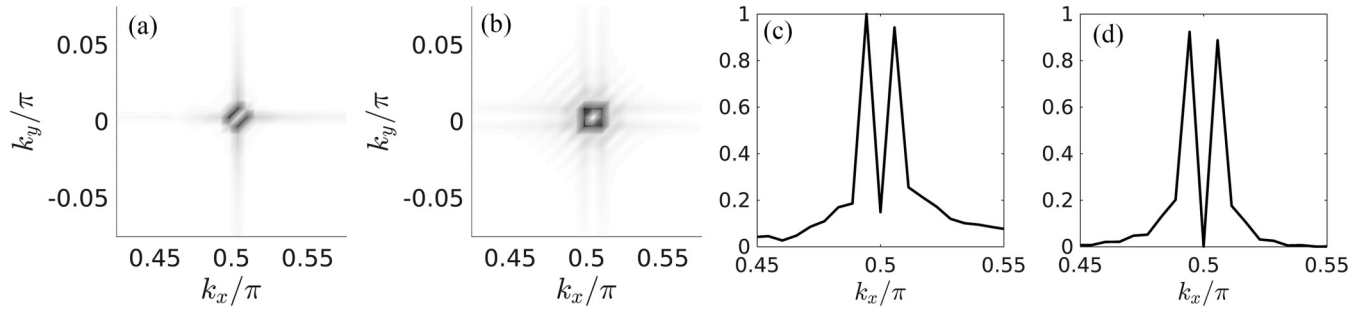

FIG. 6. Fourier transforms of the LDOS for our defects around the dominant Fourier component: $2Q\mathbf{e}_x$ (zoomed in near the CDW ordering wave vector) in the background of a half-vortex of the PDW and a double dislocation of the CDW. The density of k-points is determined by the lattice size, here $N = 400$. Top row: FT-LDOS for (a) the half-vortex and (b) the double dislocation. Notice the Fourier harmonic around the ordering wave vector vanishes/are suppressed. The split peaks are seen more clearly by plotting its amplitude along cuts in k-space. Here we have the absolute value of the FT along the line $k_y = 0$ shown for the half-vortex in (c) and for the double dislocation in (d).

dislocation *both* components of the PDW order parameter, $\Delta_{\pm\boldsymbol{Q}}$, vanish at the core, and the BdG states become gapless at there. Other details associated with LDOS of our defects can be found in Appendix D, where a zero bias probing voltages is considered.

C. Patterns of the FT of the topological defects

We now analyze in detail the effects that the half-vortex and the double dislocation have on the induced CDW order. Recall that inside the core of the half-vortex the SC order parameter is mostly FF type, since the amplitude of one of the two PDW order parameters must vanish at the location of the half-vortex, i.e., the origin (see Sec. III). Since the FF state breaks inversion symmetry in the x direction, the corresponding CDW pattern inherits this broken symmetry. Also, the edge dislocations of the CDW order parameter break inversion symmetry in the y direction. Note that the parity operator, in the x direction, changes the location of the branch cuts and the signs of the winding numbers when it acts on the order parameters, which changes the sign of the dislocation charge. As a result, the corresponding charge-density patterns are flipped on their head under this operation. Since the location of the branch cuts have no physically significant effects on the charge density, the full vortex is invariant under this operation.

The ordering wave vector $2\mathbf{Q}$ has many features made more apparent in the Fourier transforms of the LDOS, which are shown in Figs. 6(a) and 6(b). Notice that the Fourier transforms of the LDOS for half-vortex and the double dislocation feature split peaks at the $2\mathbf{Q}$ ordering wave vector where the amplitude of the FT-LDOS is zero there. In contrast, in the case of the Abrikosov vortex, the Fourier transform of the LDOS is just the transform of $\cos(2\mathbf{Q}x)$, which has a single peak at the ordering wave vector. Cuts of the FT-LDOS along $k_y = 0$ are given in Figs. 6(c) and 6(d) to more clearly illustrate these split peaks.

The split peaks are signature of the defects of the PDW phase associated with jumps in the phase θ_-, defined in Eq. (2.8), across the core of the topological defect. For example, across the half-vortex the phase jumps by $\pm\pi/2$ since it winds by π around the half-vortex. This implies that the $2Q$ Fourier component is equal to itself times i across the core of the defect, suggesting that this Fourier component must be zero. We can explicitly verify this prediction by examining the FT of $\rho_{2\mathbf{Q}}(\mathbf{r})$. It is apparent that a nonzero CDW winding number is responsible for the vanishing of $\rho_{2\mathbf{Q}}(\mathbf{r})$ at the center of the defect. In other words, the phase shift that causes this destructive interference is a measurement of the Burgers vector, which is the topological charge of the dislocation. Similar interference patterns are well known to exist in electron diffraction in crystals of semiconductors with dislocations.

Similar split peaks in the Fourier transform of the tunneling LDOS were also predicted to exist at the PDW halo of an Abrikosov vortex of a superconductor in Refs. [16,64], but their physical origin is very different. Indeed, in the case of the vortex halo there is a phase shift in the $\rho_{\mathbf{Q}}(\mathbf{r})$ (instead of $\rho_{2\mathbf{Q}}(\mathbf{r})$) Fourier component of the local charge density caused the Abrikosov vortex of the uniform component of the superconductor.

Alternatively, when there is a winding number in both PDW components, we can picture the phase jump as occurring in both winding numbers independently. Recalling the form of the induced $2Q$-CDW from Eq. (2.6), we see that complex conjugation flips the phase winding of one of the PDW components. Thus, when we have a vortex in both components $\Delta_{\pm\boldsymbol{Q}}$ with the same winding, i.e., the Abrikosov vortex, the phase differences cancel each other, and there is no net phase jump across the core of the vortex. Hence, in the case of the Abrikosov vortex there is not a split peak. Equivalently, the Abrikosov vortex does not have any dislocation charge associated with it to cause a split peak to exist. We can contrast this with the double dislocation where the phase jump adds up to π, and the amplitude at the CDW ordering wave vector should vanish by an identical argument to that of the half-vortex. We could again perform the FT to verify these results explicitly or, alternatively, argue that it should hold by way of the amount of dislocation charge associated with a given defect.

We finish this section by analyzing cuts of the real space patterns of the double dislocation and the half-vortex across the vortex cores, seen in Fig. 7. The split peaks have a clear signature in the real space patterns. Since they arise due to jumps in phase of θ_- across the vortex core, the CDW pattern in real space showcases these phase jumps. To demonstrate this we place a waveform of the defect-free PDW in

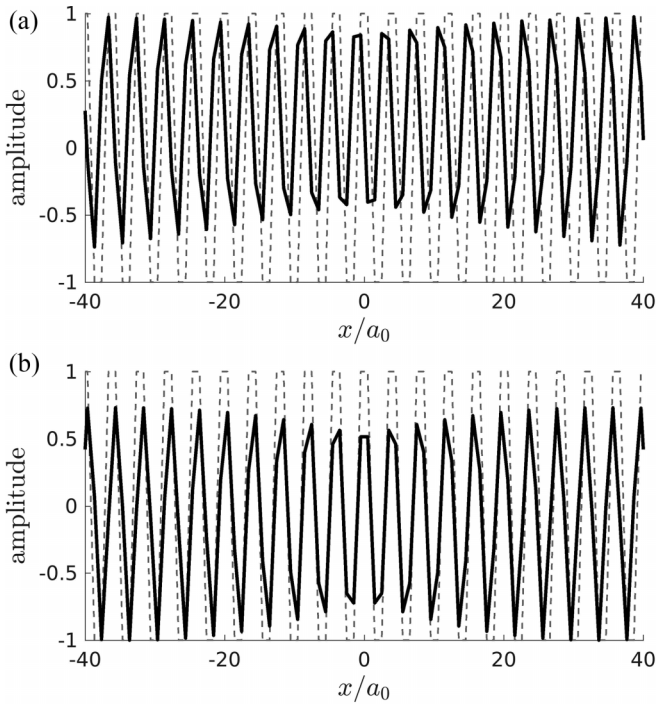

FIG. 7. Real space plots of the effects on the CDW order parameter along the x axis due to the (a) half-vortex and the (b) double dislocation. We plot these distorted CDWs on top of a CDW of a defect-free PDW state for comparison. The real space patterns show a jump in the CDW phase around the vortex core giving another physical realization of the split peaks seen in the FT-LDOS.

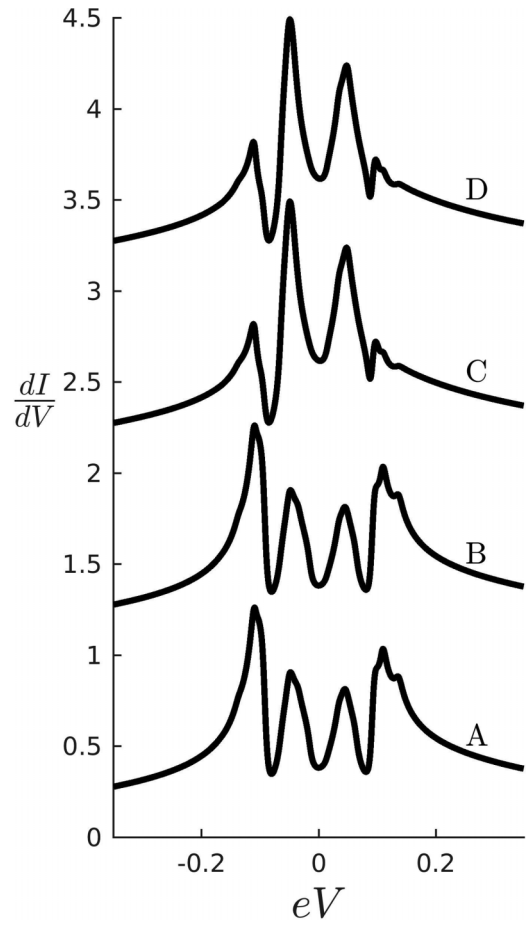

FIG. 8. Comparison of $\frac{dI}{dV}$ curves related to the electron tunneling DOS for a period 8 PDW (LO state). The electron tunneling DOS is sensitive to the periodicity of the associated period 4 CDW. The labeled *A*–*D* are the tunneling DOS traces at the four inequivalent sites of the CDW. Each consecutive curve is offset by 1 for clarity. Notice that in the PDW traces particle-hole symmetry is present only at low bias (low energies).

the background of the half-vortex and the double dislocation (dotted line).

Starting with the double dislocation we can see the π phase shift which occurs across the vortex core. The associated CDW pattern of the double dislocation has a "sawtooth" pattern, seen in Fig. 7(b), to the left and to the right of the vortex core, which is even in x being inversion symmetric. Comparison with the daughter $2Q$-CDW of the defect-free PDW gives us a subtle indication of the π phase shift. A given sawtooth pattern lies within one of the waveforms of the defect-free PDW. Sufficiently far from the core of the vortex the teeth of the saws are odd in respect to the underlying waveform, peaking on the right side of the wave on the l.h.s. and vice versa for the r.h.s. of the vortex. This is indicative of a π phase shift because the locations of the maximums and minimums of the double dislocation's CDW change their relative orientation within the square wave, and is indeed needed to maintain inversion symmetry along the x direction.

Instead, for the half-vortex [Fig. 7(a)] the induced CDW on the l.h.s. of the vortex is (basically) in phase with the background CDW. Again it is a sawtooth pattern, but the minima and maxima of the two waves coincide. Within the core of the vortex the two patterns slightly dephase from each other, and the half-vortex's CDW is zero when the defect-free PDW amplitude is at a maximum, meaning there was a $\pi/2$ phase shift. This was to be expected from the above discussion. Unlike in the case of the double dislocation the half-vortex's CDW is asymmetric about $x = 0$. This too is to be expected from the breaking of inversion symmetry.

D. Tunneling DOS spectra of the topological defects

We now compare and contrast experimental signatures associated with dI/dV curves belonging to various superconducting order parameters. These curves illustrate that the half-vortex can be thought of as an interpolation between an FF-like state (in the core) to a LO-like state (at infinity). Also, evidence of inversion symmetry breaking in the tunneling data for the half-vortex state is discussed. We also changed the energy resolution in this section to 0.01 eV to smooth out the curves and make the low bias particle-hole symmetry more apparent.

We begin with a comparison plot between the inequivalent sites for a defect-free LO state shown in Fig. 8. These plots showcase coherence peaks, like a uniform superconductor or low-bias particle-hole symmetry as well as additional satellite peaks and a zero-bias electron DOS. Additionally, the *electron* tunneling data for the PDW state are periodic with half the

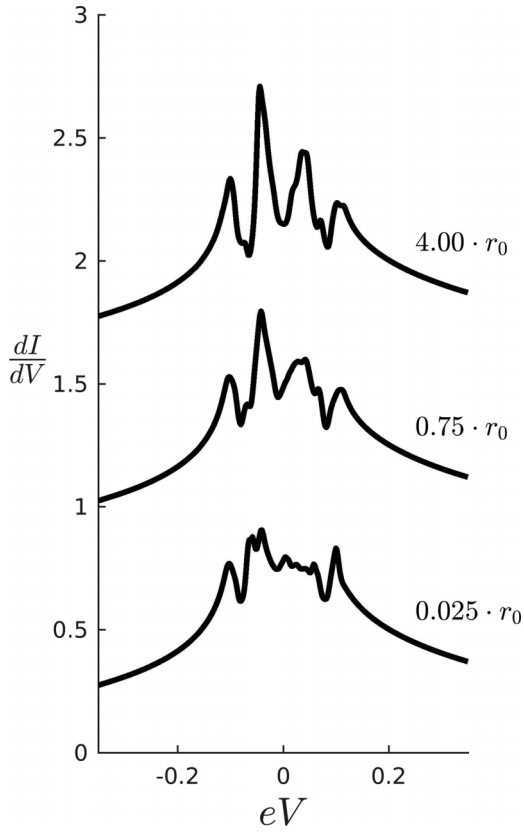

FIG. 9. A set of $\frac{dI}{dV}$ curves for the half-vortex belonging to different lattice sites. The labels indicate the distance the lattice site in question is from the vortex core in fractions of the halo radius, $r_0 = 24a_0$. The top two curves are shifted up by 0.75 and 1.5 units in respect to zero. Close to the center of the core the curves resemble a squeezed in FF state more so than an LO state, but as we move outward the coherence peaks grow, and the half-vortex behaves more like an LO state. In Appendix E, Fig. 14, additional curves corresponding to a half-vortex are provided, which indicates a four-lattice site periodicity, like the LO state, but there is also a shift in tunneling spectra associated with the jump in phase of θ_+ across the vortex core. This, along with reduced coherence peaks and additional satellites, distinguished the half-vortex from the pure PDW even far outside the vortex core.

period of the PDW since the data sense the associated CDW (for a detailed analysis see Ref. [55]), which is established by varying the x coordinate. Thus the curves have a periodicity of four lattice spacings here, and not eight like our PDW order parameter, so we label the four representative curves with letters *A*–*D*. Alternatively, the periodicity is 4, and not 8, because the remaining four lattice sites have a SC gap which is π-phase shifted in respect to the first four, and a normal metal STM tip is blind to this effect. The full periodicity of the PDW state can be detected with *pair* (Jospehson) tunneling. This will be discussed elsewhere. The defect-free FF-state (not shown) possesses a constant tunneling DOS across the entire plane, so only one representative curve is needed. Clearly then the FF state possesses data which are rotationally invariant (by $\pi/2$ in the CuO_2 planes) unlike the above LO state.

We now compare the LO states to a set of curves corresponding to the half-vortex (Fig. 9). The labels on each curve indicates how far we are from the vortex core in fractions of the halo radius, $r_0 = 24a_0$. We first note that near the core of the half-vortex the $\frac{dI}{dV}$ curve is not that of a free particle. In fact, it resembles a squeezed in FF state, even possessing the discrete rotational symmetry of the lattice (not shown). As we travel out to the edge of the vortex, the half-vortex begins to become more LO-like than FF-like. This is the interpolation from a FF to a LO state that the half-vortex undergoes, apparent from our boundary conditions in Eq. (3.16).

The presence of a half-flux quanta will further distinguish the half-vortex from the defect-free PDW far outside the vortex core. In Appendix E we provide supplementary dI/dV plots taken outside the core of the vortex, which indicated there is a relative shift in the tunneling DOS curves. Indeed, Fig. 14 in Appendix E compares the half-vortex tunneling spectrum to the right and to the left of the vortex core [Figs. 14(a) and 14(b), respectively]. Again there is a periodicity present (outside the vortex core) in these plots, and just like an LO state, the dI/dV curves repeat every four lattice spacings. It should also be noted that the curves presented in the Appendix have a defect which is placed on the CuO_2 bonds opposed to at the center of the plaquette. This changes the appearance of the dI/dV curves, but the spectral weight associated with the quasiparticles remains the same. That is, we shifted the period 4 CDW by half a lattice spacing, which costs us no, or very little, energy to do so.

The half-vortex becomes more LO-like outside the core of the half-vortex, but since this topological defect breaks inversion symmetry, its tunneling DOS must reflect this, unlike the LO state. A smoking gun signature of inversion symmetry breaking is present by comparing the dI/dV curves to the left and to the right of the vortex core [Figs. 14(a) and 14(b), respectively]. It is apparent the data on the left are two lattice spacings behind the right (or vice versa), which we attribute to the jump in θ_+ by $\pi/2$ across the vortex core. Indeed, the accumulated phase belonging to a Cooper pair with nonzero COM momentum: $\mathbf{Q} \cdot \mathbf{r} = \pi/2$ if $\mathbf{r} = 2a_0\mathbf{e}_x$. We will see another example of inversion symmetry breaking in the next section when we discuss the spectral functions for the half-vortex. This jump in phase distinguishes the half-vortex from a defect-free LO state, even outside the half-vortex core.

Note the full vortex also possesses a phase jump of $\Delta\theta_+ = \pi$ across the vortex core, but this gives a relative shift of four lattice spacings when comparing electron tunneling DOS on the left and right hand sides of the full vortex. This means there is no analogous signature belonging to the full-vortex as there was for the half-vortex when using a normal metal tip. This is simply because the LO state has the same periodicity as this shift. On the other hand, in the case of a superconducting tip there will be a difference in the pair tunneling DOS on the right- and left-hand sides of the full vortex. Finally, we note that the presence of a gap in the core of the half-vortex distinguishes it from the other two topological defects since the latter two have a vanishing gap here. This results in a free particle tunneling DOS in the core of the defect for the double dislocation and the full vortex opposed to a squeezed in FF state seen in the core of the half-vortex [see Fig. 15(a) in Appendix E]. Finally, we can see in Fig. 15(b)

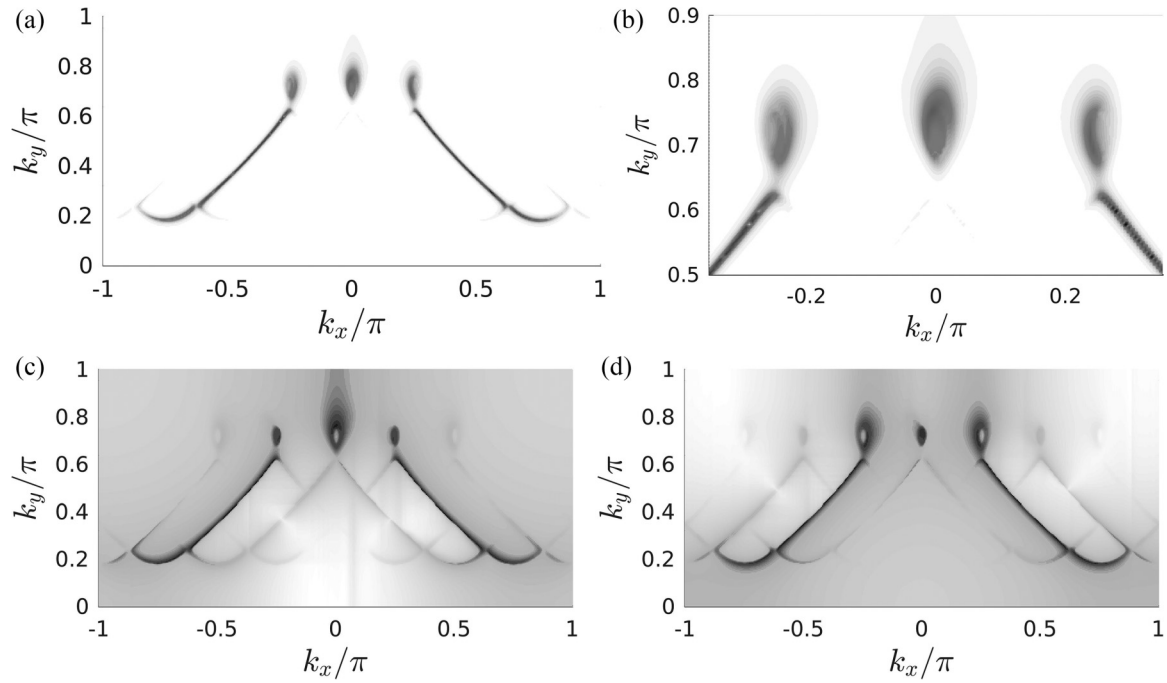

FIG. 10. The Bogoliubov Fermi surface, $A(\mathbf{k}, \omega = 0)$, for a PDW state with a half-vortex of radius $r_0 = 24a_0$ and a d-wave form factor. In (a) we plot the upper portion of the Bogoliubov Fermi surface, which indicates a redistribution of spectral weight in respect to the defect-free PDW (see Appendix F for plots). In (b) we zoom in on these loops, which indicate inversion symmetry breaking. We also partition the Fermi surface of the half-vortex into (c) the particlelike portion and (d) the holelike portion. Notice the intensity of the spectral weight belonging to the Fermi arcs tends to be either particlelike or holelike depending on the side you are on.

that the half-vortex possesses additional satellites peaks past these other two defects, and so the full-vortex and the double dislocation more closely resemble the pure PDW outside the core. The inequivalent gaps corresponding to the distinct Fourier components of the half-vortex is responsible for these additional satellites.

E. Spectral functions

In this section we analyze the spectral functions of the PDW state in the presence of topological defects, again, paying special attention to the half vortex. We will also be particularly interested in the plots of the spectral function $A(\mathbf{k}, \omega = 0)$, defined in Eq. (4.5), which counts how many quasiparticle states are connected to the ground state within our energy resolution, ϵ. In a metal the spectral function at zero frequency yields the locus of points corresponding to the Fermi surface in the Brillouin zone. In the case of a PDW the spectral function at zero frequency reveals the locus of the Fermi surface of the Bogoliubov quasiparticle. Here we will use the term *Bogoliubov Fermi surface* to represent the locus of points on the Brillouin zone where there are pockets of Bogoliubov quasiparticle. Since the Bogoliubov quasiparticles are admixtures of electrons and holes different portions of the Bogoliubov Fermi surfaces have electron or holelike character. Still we expect some resemblance between the Fermi surface of the normal state and the Bogoliubov Fermi surfaces of the PDW states; we give more on this below.

The Bogoliubov Fermi surfaces of the PDW state have been examined in Refs. [25,46] and in a quasi-1D model of the PDW in Ref. [39]. In these references it was shown that in a time-reversal invariant superconductor, such as the PDW with wave vector $\boldsymbol{Q}$, the pockets are separated by gaps in k-space, where the SC gap is nonzero, where the condition $\xi_{\mathbf{k}} = \xi_{\mathbf{k}\pm\mathbf{Q}}$ is satisfied; here $\xi_{\mathbf{k}}$ is the quasiparticle dispersion in the nonsuperconducting state. These gaps appear where the Fermi surface of the normal state is perfectly nested, and we pair electrons with their time-reversed partner.

In this subsection we are interested in the effects of the topological defects on the spectral functions of a PDW. A plot of a few Fermi surfaces of Bogoliubov quasiparticle of the PDW in the presence of a half-vortex can be found in Fig. 10. Here we consider a half-vortex of $r_0 = 24a_0$ possessing a d-wave form factor. Spectral plots of a pristine PDW with both an s-wave and d-wave form factor as well as log plots of the Abrikosov vortex and the double dislocation (both with d-wave form factors) can be found in Appendix F, Fig. 16. The latter two plots greatly resemble the spectral function of the pure PDW, small differences only becoming apparent on taking a logarithm. As in the spectral functions of the defect-free PDW of Ref. [25] the portion of the Bogoliubov Fermi surfaces closely resemble "arcs" along the ungapped parts of the normal Fermi surface (i.e., in the absence of the PDW state).

We first observe that the normal state dispersion is partially retained for the presence of the half-vortex. This also holds true for the other defects and is illustrated in Appendix F, Fig. 16, where we also overlaid a copy of the normal state Fermi surface with that of the pure PDW [Fig. 16(b)]. These gapless regions retain the normal state character [48]. Utilizing the weak coupling argument above we realize the modified

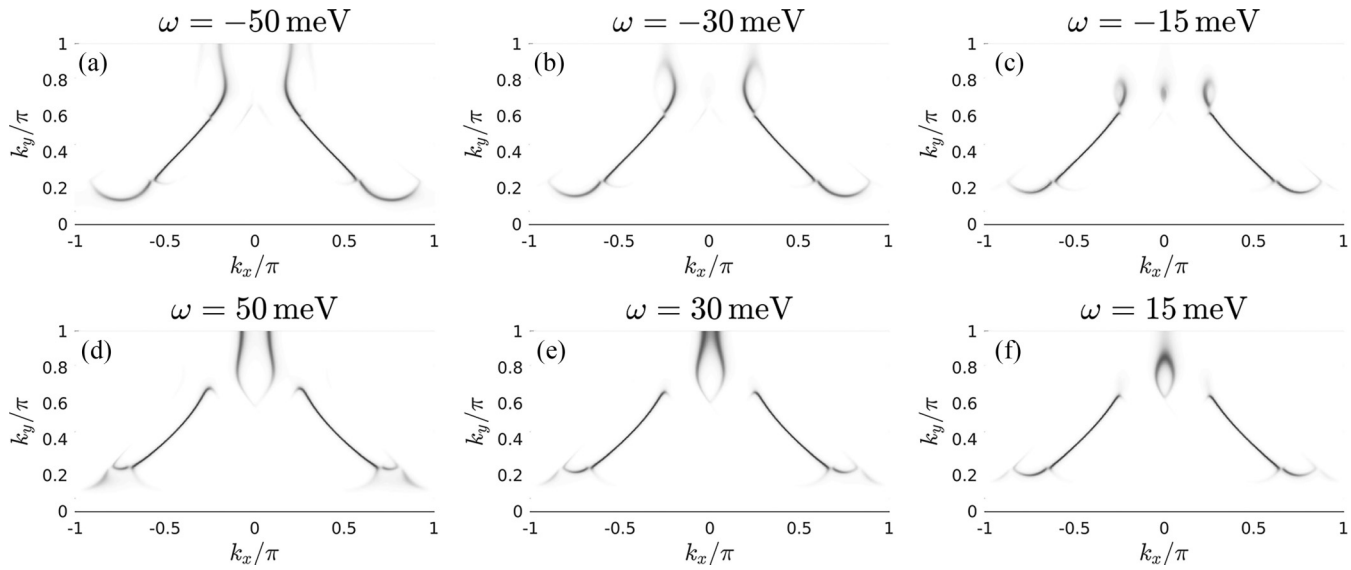

FIG. 11. The spectral function, $A(\mathbf{k}, \omega)$, of the PDW with a half-vortex ($r_0 = 24a_0$) evaluated at various energies: ω. From plots (a)–(f) we can see the holelike character grows with a negative bias and the particlelike portions with positive bias. This redistribution of spectral weight can be used to map out the dispersion.

nesting condition suggests an *s*-wave form factor would also possess these Fermi arcs [see Fig. 16(a)].

The most striking feature of the spectral function in a PDW with a half-vortex is the redistribution of spectral weight to regions above the arcs forming discernible loops seen in Fig. 10(a). In Fig. 10(b) we zoom in on these loops to indicate a degree of inversion symmetry breaking, seen in the distribution of spectral weight in these loops and along the arcs. Inversion symmetry is broken in the core of the half-vortex where the SC state becomes close to that of an FF state. Note that the formation of these loops does not occur so dramatically for the other two topological defects, but it still happens to some degree. The half-vortex is special in the sense that it couples to both the CDW and the SC degrees of freedom, unlike the other two topological defects. The asymmetry in the charge density induces a significant reshuffling of the spectral weight for the half-vortex according to these plots.

A point worth mentioning at this stage is the apparent coexistence of the "Fermi arcs," just mentioned, and electron/hole pockets [65]. An arc usually refers to a large section of the Fermi surface which is seemingly open-ended. The pockets on the other hand are small closed surfaces. An experimental probe known as angle-resolved photoemission spectroscopy (ARPES) can help determine the Fermi surface, but the holelike regions are invisible to ARPES [66]. We can demonstrate this by looking at log plots of the particlelike Fermi surface [Fig. 10(c)] and the holelike Fermi surface [Fig. 10(d)]. Here it can be seen that the front and backsides of these arcs have primarily particlelike or holelike character, respectively. Note that this is the case for all the other PDW order parameters as well.

We can further examine the holelike and particlelike character of certain regions of the Bogoliubov Fermi surface in the presence of the half-vortex by looking at the spectral function for various probing voltages [Figs. 11(a)–11(f)]. We see the spectral weight shifts around from one set of loops to another depending on the sign of the bias. Indeed, Fig. 11 demonstrates a negative bias will grow the holelike loops of the Fermi surface, while positive biases the electronlike portions. This redistribution of spectral weight pertains to the fact holes are at a negative energy in respect to the Fermi energy and vice versa for the particles.

V. DISCUSSION AND CONCLUSIONS

Evidence for the existence of pair density wave superconducting phases (or at least a PDW component) has continued to grow. In addition to the panoply of evidence in the cuprate superconductors [2] new evidence for PDW order has now been found in other materials such as the heavy fermion superconductor UTe_2 [17,18], in a monolayer iron superconductor Fe(Te,Se) [19], in $EuRbFe_4As_4$ [20], and in the kagome superconductor CsV_3Sb_5 [22]. This growing body of evidence of the existence of PDW superconducting states makes the characterization of these phases an important problem.

In this paper we investigated the electronic structure of the BdG Hamiltonian of a unidirectional PDW in two dimensions in the presence of its three topological defects: the half-vortex, the Abrikosov vortex, and the double dislocation. In essence we showed that the topological defects of a PDW generically have "halos" which provide evidence for the nature of this superconducting state. However, it is important to distinguish the halos of the PDW topological defects, which occur *in the absence* of a magnetic field, to the PDW halo of a superconducting vortex, which requires *the presence* of a magnetic field [15,16,64]. In contrast, the half-vortex and double dislocation topological defects of the PDW can be created only by impurities.

This work was partly motivated by evidence for half vortices found by Du and collaborators [14] in STM experiments in the superconducting state of the high T_c superconductor $Bi_2Sr_2CaCu_2O_{8+\delta}$. The results of our work will also be useful for investigating in the PDW superconducting state the heavy

fermion superconductor UTe_2. Recent STM experiments in this material have revealed that in its vortices the associated CDW has a dislocation-antidislocation dipole structure [67]. Our results provide alternative ways to investigate the nature of the PDW superconductors by investigating the structure of its interesting topological defects.

For practical reasons the PDW was taken to be commensurate with the lattice spacing of the CuO_2 planes with a periodicity of $8a_0$. The restriction to a commensurate PDW was needed for our numerics. However, in a truly commensurate PDW topological defects such as the half-vortex and the double dislocation have a linearly divergent energy instead of a logarithmic divergent energy for an incommensurate PDW. Also, in the presence of a uniform component of the d-wave superconducting order the half-vortex also has a linearly divergent energy. We have not discussed this case here. Nevertheless, in both cases half vortices can appear in the vicinity of static impurities. At any rate, a nearly commensurate PDW looks like a locally commensurate state with *discommensurations* to account for the incommensurate character. The same physics is know to occur in conventional CDW states [68]. This is also what is seen in STM experiments in the cuprate superconductor $Bi_2Sr_2CaCu_2O_{8+\delta}$ where the observed CDW order is locally commensurate [58].

The PDW state and its topological defects was treated using the Landau-Ginzburg theory of the Refs. [1,25,26], which describes the PDW and its CDW as intertwined orders. In this approach, the CDW order parameter is a composite operator of the two independent PDW order parameter fields. The static configuration of the half-vortex was derived using a nonlinear sigma model approximation valid deep in the PDW phase. The BdG Hamiltonian of the PDW was then adapted to include the changes in the PDW order parameter in the presence of the topological defects. The calculation of the electronic states described by the BdG Hamiltonian is not self-consistent. Using the resulting Green functions of our effective theory, obtained numerically, we investigated the $4a_0$ CDW of the PDW phase as well as the effects of the topological defects on the electronic states. We should note that this approach is not self-consistent since the PDW order parameter (with or without defects) is fixed. The lack of self-consistency require some caveats on our results that are discussed below.

The half-vortex of the PDW is particularly interesting as it is essentially a dislocation of the CDW order parameter pinned to a half-flux quantum of the superconductor [2,25,44,45]. In this paper we investigated several aspects of the core of the half-vortex. We showed that the half-vortex of the PDW, which is an LO type state, has a "halo" of an FF state. This FF state causes inversion symmetry to be broken at the core. Another interesting effect that arises in the presence of a half-vortex is the splitting of the peaks of the associated CDW at the ordering wave vector $2\mathbf{Q}$. The split peak arises from a $\pi/2$-phase shift across the half-vortex core. We verified this explicitly via examination of the Fourier transform of the LDOS. On the other hand, the double dislocation is also shown to exhibit a split peak, which is due to a π-phase shift across its core. As expected, we found that there is no such split peak seen in the Abrikosov vortex consistent with the fact that this topological defect does not involve a dislocation of the CDW order of any type.

We analyzed in detail the quasiparticle spectral function of a PDW with a half-vortex defect. In addition to the "arclike" structure at the Fermi surface of the Bogoliubov quasiparticle states which are seen in the defect-free PDW state [25,46], we found that the half-vortex induces asymmetric "looplike" structures above the "arcs." We attributed the existence of these loops to the breaking of inversion symmetry at the core of the half-vortex. While much of the quasiparticle spectral function is very similar to that of the defect-free PDW, the presence of the half-vortex, and its inversion symmetry breaking, has a clear imprint in the spectral function. We also analyzed the real space position and the voltage dependence of the local differential conductance across a half vortex core. This dependence gives additional evidence for the existence of an FF component of the PDW in the core of the half-vortex.

Since this is not a self-consistent theory, both the spectral functions and the differential tunneling conductance results should be reliable at low energies but cannot be trusted at energies (voltages) substantially higher than the superconducting gap. As a matter of principle we expect that at energies well above the gap the superconducting order parameter should be progressively suppressed and the Bogoliubov quasiparticle effectively should become "normal" electrons. This also implies that the composite order parameters such as the CDW should also be progressively suppressed well above the gap. This is not what happens in our numerics, which computed the BdG spectrum in a fixed background of the superconducting order. To have a fully self-consistent theory requires a viable physical mechanism for a PDW which cannot be obtained by a weak coupling BCS-type theory. This is an open problem and a matter of current research.

In most systems in which PDW has been observed it happens in, at best, coexistence with a uniform superconducting state. This happens even in the case of $La_{2-x}Ba_xCuO_4$, which has, so far, provided the best evidence for PDW order (see Refs. [2,69] and references therein). Thus it is important to understand what changes are brought about to our results when a PDW coexists with uniform superconducting order parameter. We plan to address this problem in a separate publication.

Contrary to the case of vortices in a superconductor, whose number and separation are controlled by an external magnetic field, impurities are needed to create the half-vortices and double dislocations of a PDW. Here we considered the problem of single isolated topological defects. In practice this will require very clean systems so that the impurities are separated over large distances, larger than the size of the halos. On the other hand, a finite density of disorder has large qualitative effects in states such as the PDW, including the destruction of long-range CDW order [70,71], and most intriguingly a possible charge-4e superconducting state [44] by proliferation of double dislocations as proposed in Ref. [72]. These important open problems are beyond the scope of this paper.

ACKNOWLEDGMENTS

We thank Ryan Levy, Raman Sohal, and Yuxuan Wang for useful discussions pertaining to the setup of the numerical

simulation. Furthermore, we thank Peiyan Wu for his help in parallelizing the eigensolvers and for correcting the orthogonalization algorithms in these canned routines. M.R. thanks Mike Stone with his help in clarifying certain aspects of our solution process. This work was supported in part by the U.S. National Science Foundation through Grant No. NSF DMR 2225920 at the University of Illinois (M.R. and E.F.) and by the (2017) Sloan Foundation (M.R.).

APPENDIX A: BOGOLIUBOV-VALATIN TRANSFORMATION

Here we outline the solution process of the following Bogoliubov–de Gennes (BdG) Hamiltonian:

$$\hat{H} = -\sum_{i,j,\sigma} t_{ij}\hat{c}^{\dagger}_{i\sigma}\hat{c}_{j\sigma} + \sum_{i,j}(\tilde{\Delta}_{ij}\hat{c}^{\dagger}_{i\uparrow}\hat{c}^{\dagger}_{j\downarrow} + \text{H.c.}). \tag{A1}$$

We associate each Latin index with position in this Appendix. It is standard to diagonalize this operator using a Bogoliubov-Valatin (BV) transformation, but we will opt for a Nambu formalism instead. In the end we obtain the same BV transformation defining the same quasiparticles; the alternative route of defining our quasiparticle operators before diagonalizing can be found in Ref. [73].

Let's define the following operator: $\tilde{\psi}^T = [\mathbf{c}_{\uparrow}, \mathbf{c}_{\downarrow}]$, where the above components are vectors that consist of electron operators, $[\mathbf{c}_{\sigma}]_i = \hat{c}_{\mathbf{r}_i\sigma}$. Defining our Nambu spinor as $\tilde{\Psi}^T = [\tilde{\psi}, \tilde{\psi}^{\dagger}]$ we can express our above Hamiltonian as a matrix product

$$\hat{H} = \tilde{\Psi}^{\dagger}\tilde{\mathbf{H}}\tilde{\Psi} = \tilde{\Psi}^{\dagger}(\tilde{\mathbf{V}}\mathbf{E}\tilde{\mathbf{V}}^{-1})\tilde{\Psi} \equiv \tilde{\gamma}^{\dagger}\mathbf{E}\tilde{\gamma}. \tag{A2}$$

The explicit definitions of the terms presented in Eq. (A2) will be covered in the next few paragraphs, but essentially this is just a similarity transformation. The matrix $\tilde{\mathbf{H}}$ takes the following generic form:

$$\tilde{\mathbf{H}} = \frac{1}{2}\begin{bmatrix} \mathbf{T} & \tilde{\mathbf{\Delta}} \\ \tilde{\mathbf{\Delta}}^{\dagger} & -\mathbf{T}^T \end{bmatrix}. \tag{A3}$$

Defining $[\mathbf{t}]_{ij} = -t_{ij}$ and $\mathbf{\Delta}_{\uparrow\uparrow}/\mathbf{\Delta}_{\uparrow\downarrow}$ (etc.) for triplet/singlet superconductivity we have the following forms for our submatrices:

$$\mathbf{T} = \begin{bmatrix} \mathbf{t} & \mathbf{0} \\ \mathbf{0} & \mathbf{t} \end{bmatrix}, \quad \tilde{\mathbf{\Delta}} = \begin{bmatrix} \mathbf{\Delta}_{\uparrow\uparrow} & \mathbf{\Delta}_{\uparrow\downarrow} \\ \mathbf{\Delta}_{\downarrow\uparrow} & \mathbf{\Delta}_{\downarrow\downarrow} \end{bmatrix} = -\tilde{\mathbf{\Delta}}^T. \tag{A4}$$

This last condition on the SC matrix is a consequence of the anticommutation relations, and the formation of this matrix should be chosen such that the above product reproduces the original Hamiltonian.

We next define the quasiparticle operators, $\tilde{\gamma} = [\mathbf{b}^{\dagger}, \mathbf{b}]^T$, which can be expressed in terms of the electron creation and annihilation operators with the unitary matrix inducing the similarity transform, $\tilde{\mathbf{V}}$. Our similarity transform takes a very simple form because there are no zero modes in our spectrum due to the finite size of the system (needed for numerical diagonlization). This reveals we have $\pm$ energy pairs, and they are related via complex conjugation of the eigenvalue equation and swapping the top blocks of the BdG equations with the bottom. That is, given (sorted) eigenenergies $E_l > 0$ ($l \in \{1, \ldots, 2N^2\}$) we have the corresponding negative energy solutions

$$\tilde{\mathbf{H}}\begin{bmatrix} \tilde{\mathbf{u}}_l \\ \tilde{\mathbf{v}}_l \end{bmatrix} = E_l\begin{bmatrix} \tilde{\mathbf{u}}_l \\ \tilde{\mathbf{v}}_l \end{bmatrix} \quad \Rightarrow \quad \tilde{\mathbf{H}}\begin{bmatrix} \tilde{\mathbf{v}}^*_l \\ \tilde{\mathbf{u}}^*_l \end{bmatrix} = -E_l\begin{bmatrix} \tilde{\mathbf{v}}^*_l \\ \tilde{\mathbf{u}}^*_l \end{bmatrix}. \tag{A5}$$

We now define the following $2N^2 \times 2N^2$ matrix $\tilde{\mathbf{u}}$ by setting it's lth column equal to $\tilde{\mathbf{u}}_l$, and similarly for $\tilde{\mathbf{v}}$, so the row index corresponds to the lattice site and the matrix $[\mathbf{E}]_{lk} = E_l\delta_{lk}$. The unitary matrix inducing the similarity transform takes the following form:

$$\tilde{\mathbf{V}} = \begin{bmatrix} \tilde{\mathbf{v}}^* & \tilde{\mathbf{u}} \\ \tilde{\mathbf{u}}^* & \tilde{\mathbf{v}} \end{bmatrix}. \tag{A6}$$

The block matrices, $\tilde{\mathbf{u}}$ and $\tilde{\mathbf{v}}$, contain the real space coherence factors, and provide us with the following electron operators in terms of our quasiparticle operators:

$$\begin{aligned} \hat{c}_{i\uparrow} &= \tilde{v}^*_{il}\hat{b}^{\dagger}_l + \tilde{u}_{il}\hat{b}_l, \quad \hat{c}^{\dagger}_{i\uparrow} = \tilde{v}_{il}\hat{b}_l + \tilde{u}^*_{il}\hat{b}^{\dagger}_l, \\ \hat{c}^{\dagger}_{i\downarrow} &= \tilde{u}^*_{il}\hat{b}^{\dagger}_l + \tilde{v}_{il}\hat{b}_l, \quad \hat{c}_{i\downarrow} = \tilde{u}_{il}\hat{b}_l + \tilde{v}^*_{il}\hat{b}^{\dagger}_l, \end{aligned} \tag{A7}$$

We can substitute these into our Hamiltonian above, and we find

$$\hat{H} = \sum_{E_l>0} E_l\hat{b}^{\dagger}_l\hat{b}_l + E_G. \tag{A8}$$

The explicit form for E_G and $|G\rangle$ will not matter for what follows. The ground state is taken to satisfy

$$\hat{b}_l\,|G\rangle = 0. \tag{A9}$$

Defining $S_{ij} = \tilde{v}^*_{il}(\tilde{u}^*)^{-1}_{lj}$, it can be shown the ground state is a coherent state of Cooper pairs; that is, it is related to the vacuum state, $|0\rangle$, in the following way:

$$|G\rangle = \mathcal{N}\exp\left(\tfrac{1}{2}\hat{c}^{\dagger}_{i\uparrow}S_{ij}\hat{c}^{\dagger}_{j\downarrow}\right)|0\rangle. \tag{A10}$$

What we'll need below is the single-particle excited states

$$\hat{H}\hat{b}^{\dagger}_l\,|G\rangle = (E_G + E_l)\hat{b}^{\dagger}_l\,|G\rangle. \tag{A11}$$

These above relations are the building blocks of our Green functions, found in Appendix C. Before deriving those expression, it is advantageous to reconfigure our Hamiltonian for the case of a singlet SC because this will be computationally more efficient.

APPENDIX B: NUMERICAL SETUP FOR THE DIAGONALIZATION OF THE BOGOLIUBOV–de GENNES EQUATIONS

This Appendix outlines the setup for numerical diagonalization of the BdG Hamiltonian introduced in the last Appendix. When we are considering a singlet SC, we can simplify the superconducting matrix to the following form:

$$\tilde{\mathbf{\Delta}} = \begin{bmatrix} \mathbf{0} & \mathbf{\Delta} \\ -\mathbf{\Delta} & \mathbf{0} \end{bmatrix}, \quad \mathbf{\Delta}^T = \mathbf{\Delta}. \tag{B1}$$

It pays to change the basis of our Nambu spinor, so we can work with an effective Hamiltonian of half the dimension of both our column and row space. We define

$$\Psi = [\mathbf{c}_{\uparrow}\ \mathbf{c}^{\dagger}_{\downarrow}\ \mathbf{c}_{\uparrow}\ \mathbf{c}^{\dagger}_{\uparrow}]^T = \mathbf{O}\tilde{\Psi} \Rightarrow \hat{H} = \Psi^{\dagger}\mathbf{V}\mathbf{E}\mathbf{V}^{\dagger}\Psi. \tag{B2}$$

The orthogonal transformation in question takes the following simple form and gives an explicit relation between the similarity transforms in question:

$$\mathbf{O} = \begin{bmatrix} \mathbf{I} & \mathbf{0} & \mathbf{0} & \mathbf{0} \\ \mathbf{0} & \mathbf{0} & \mathbf{0} & \mathbf{I} \\ \mathbf{0} & \mathbf{I} & \mathbf{0} & \mathbf{0} \\ \mathbf{0} & \mathbf{0} & \mathbf{I} & \mathbf{0} \end{bmatrix}, \quad \tilde{\mathbf{V}} = \mathbf{O}^T \mathbf{V}. \tag{B3}$$

Defining the following matrices:

$$\mathbf{H}_{\pm} = \begin{bmatrix} \mathbf{t} & \pm\boldsymbol{\Delta} \\ \pm\boldsymbol{\Delta}^{\dagger} & -\mathbf{t} \end{bmatrix}, \tag{B4}$$

we find that our transformed Hamiltonian takes the following form [$\psi_{\pm}$ are defined inline according to Eq. (B2)]:

$$\mathbf{H} = \mathbf{O}\tilde{\mathbf{H}}\mathbf{O}^T = \begin{bmatrix} \mathbf{H}_{+} & \mathbf{0} \\ \mathbf{0} & \mathbf{H}_{-} \end{bmatrix}, \quad \Psi = \begin{bmatrix} \psi_{+} \\ \psi_{-} \end{bmatrix}. \tag{B5}$$

The matrix is block diagonal, meaning we can diagonalize the two sub-Hamiltonians independently. The eigenvectors of the lower block are related to those of the upper via the same transformation shown in Eq. (A5). In addition to this, the energies of each block come in $\pm$ pairs. This can be seen by complex conjugating the eigenvalue equations defined by Eq. (B4), then applying the following orthogonal matrix: $\mathbf{O}' = \left[\begin{smallmatrix} \mathbf{0} & \mathbf{I} \\ -\mathbf{I} & \mathbf{0} \end{smallmatrix}\right]$.

Solving one of these subblocks is enough. After doing so, and organizing our eigenvectors from least to greatest (in energy), we arrive at the following similarity transforms:

$$\mathbf{V}_{+} = \begin{bmatrix} \mathbf{v}^* & \mathbf{u} \\ -\mathbf{u}^* & \mathbf{v} \end{bmatrix}, \quad \mathbf{V}_{-} = \begin{bmatrix} \mathbf{v}^* & -\mathbf{u} \\ \mathbf{u}^* & \mathbf{v} \end{bmatrix}$$
$$\Rightarrow \quad \mathbf{V} = \begin{bmatrix} \mathbf{V}_{+} & \mathbf{0} \\ \mathbf{0} & \mathbf{V}_{-} \end{bmatrix}. \tag{B6}$$

Thus, we can simply diagonalize $\mathbf{H}_{+}$, then use our above string of relations to find the coherence factors given in the previous Appendix if needed. We work with these coherence factors defined above in the following Appendix.

APPENDIX C: RETARDED GREEN FUNCTION AT ZERO TEMPERATURE

Using the results laid out in the previous Appendixes we can find the retarded zero temperature Green functions. We start with the real space retarded Green function at zero temperature

$$G_{\sigma}(\mathbf{r}_i, \mathbf{r}_j, t) = -i\theta(t)\langle\{\hat{c}_{\mathbf{r}_i\sigma}(t), \hat{c}^{\dagger}_{\mathbf{r}_j\sigma}\}\rangle$$
$$= -i\theta(t)\langle\{e^{i\hat{H}t}\hat{c}_{\mathbf{r}_i\sigma}e^{-i\hat{H}t}, \hat{c}^{\dagger}_{\mathbf{r}_j\sigma}\}\rangle.$$

Using the action of our quasiparticle operators on our ground state, and relation Eq. (A7) or Eq. (B6), we can evaluate these terms. Recall that we are in the singlet configuration, so we may work with a single spin, say, $\sigma = \uparrow$, and drop the spin label:

$$G(\mathbf{r}_i, \mathbf{r}_j, t) = -i\theta(t)\sum_{E_l>0}(v_{il}v^*_{jl}e^{iE_lt} + u^*_{il}u_{jl}e^{-iE_lt}).$$

We are interested in the Fourier transform, which takes us from the time domain to the frequency domain. This integral requires a dampening factor, ϵ, for convergence, which represents the energy resolution, taken to be 2.5 meV. The Fourier transform gives us the Green function in a familiar form:

$$G(\mathbf{r}_i, \mathbf{r}_j, \omega) \equiv \int_{-\infty}^{\infty} G(\mathbf{r}_i, \mathbf{r}_j, t)e^{i(\omega+i\epsilon)t}dt$$
$$= \sum_{E_l\geqslant 0}\left(\frac{u_{il}u^*_{jl}}{\omega - E_l + i\epsilon} + \frac{v^*_{il}v_{jl}}{\omega + E_l + i\epsilon}\right) \tag{C1}$$

We'll also need to Fourier transform to k-space to obtain the spectral function

$$G(\mathbf{k_a}, \mathbf{k_b}, \omega) = \frac{1}{N}\sum_{i,j} G(\mathbf{r}_i, \mathbf{r}_j, \omega)e^{i\mathbf{k_a}\cdot\mathbf{r_i}}e^{-i\mathbf{k_b}\cdot\mathbf{r_j}}$$
$$= \sum_{E_l\geqslant 0}\left(\frac{\tilde{u}_l(\mathbf{k_a})\tilde{u}^*_l(\mathbf{k_b})}{\omega - E_l + i\epsilon} + \frac{\tilde{v}_l(\mathbf{k_b})\tilde{v}^*_l(\mathbf{k_a})}{\omega + E_l + i\epsilon}\right). \tag{C2}$$

With the same definition as in the text for the coherence factors

$$\tilde{u}_l(\mathbf{k}) = \frac{1}{N}\sum_i u_{il}e^{i\mathbf{k}\cdot\mathbf{r_i}},$$
$$\tilde{v}_l(\mathbf{k}) = \frac{1}{N}\sum_i v_{il}e^{i\mathbf{k}\cdot\mathbf{r_i}}.$$

APPENDIX D: PLOTS OF ρ_{2Q} AND THE LDOS

This Appendix provides comparison plots between the induced CDW for our three defects using Eq. (2.6) directly. We still see the signatures of the defects described in the text (e.g., a edge dislocation). Representative plots of the ρ_{2Q} are shown in Fig. 3. Comparison plots to the LDOS at zero bias are shown in Figs. 12(a)–12(c). Note that the core of the vortex is noticeably different in Fig. 3 than in Fig. 12 for the subplots which correspond to the full vortex and the double dislocation. This is due to the fact the LDOS calculation possesses information regarding the quasiparticles, and the patterns are a result of quasiparticle interference. The half-vortex looks similar in both these figures because its core contains a fully gapped FF state. On the other hand, the other two defects, the full vortex and the double dislocation, possess order parameters with a vanishing superconducting gap at the core. The integrated LDOS (the charge density) for the full vortex and the double dislocation also possesses a nonzero weight within the vortex core due to the fact the vortex can accommodated quasiparticles, but the dynamic features are integrated out. In Figs. 12(d)–12(f) we also provide a set of LDOS at a bias of $0.75\bar{\Delta}$. Notice the depletion of states that occurs in the core

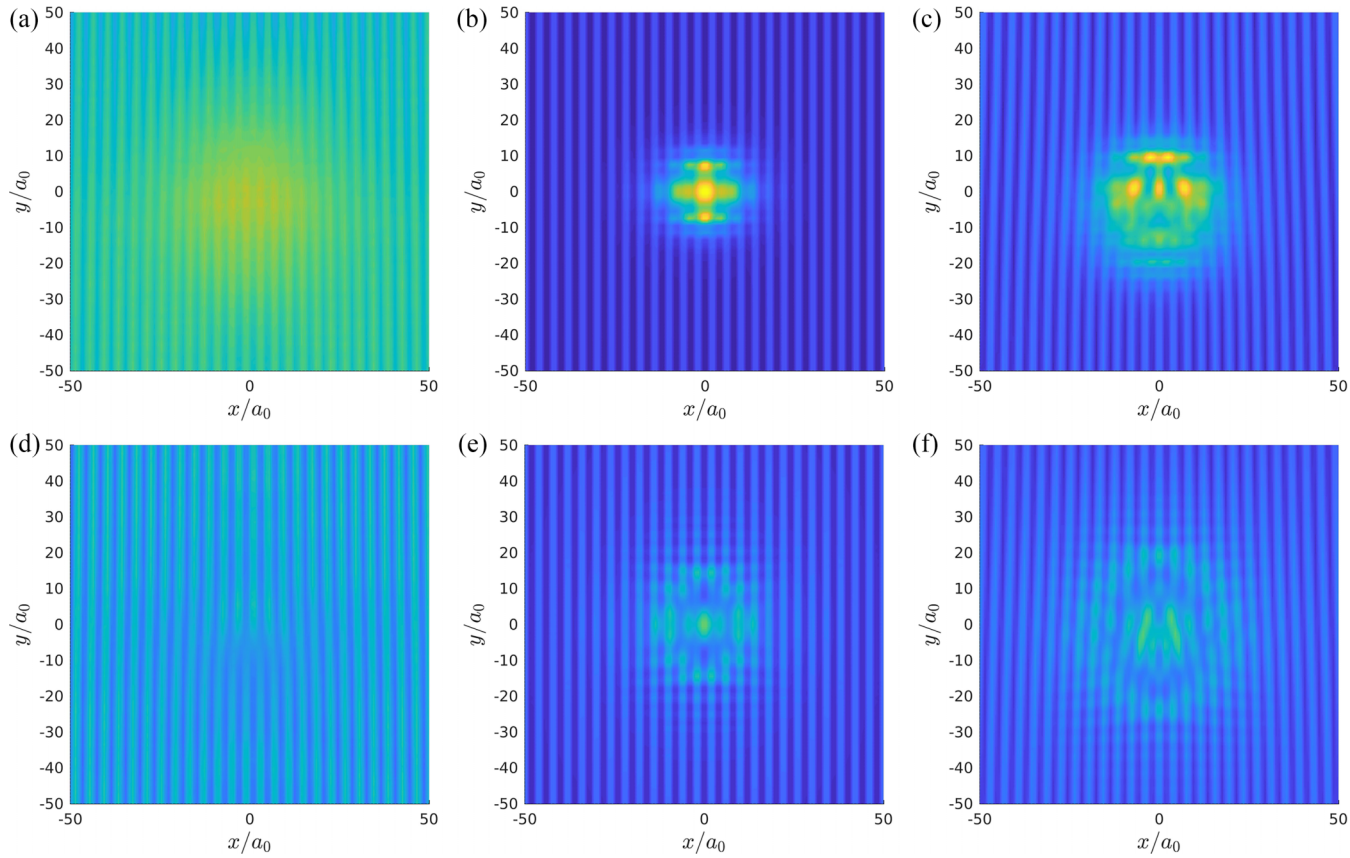

FIG. 12. Comparison plots of the LDOS for a PDW order SC with the three topological defects [described in Eq. (4.2)]. First, we consider the zero bias LDOS given in the first row for (a) the half-vortex, (b) the Abrikosov vortex, and (c) the double dislocation. In the second row we include plots of the LDOS at probing voltages of $0.75\bar{\Delta}$ for (d) the half-vortex, (e) the Abrikosov vortex, and (f) the double dislocation. Each plot is normalized to the scale of the defect as in the main text.

of the vortex even in the case of a half-vortex where there is a partial gap present.

Note these quasiparticles do not reside solely in the vortex core and are thus not bound states. We can illustrate this by taking a FT of the LDOS and plotting cuts in momentum space over a range of energies to observe a dispersion relation. The nonzero Fourier harmonics at each energy, ω, corresponds to the scattering wave vectors connecting different regions of the surface determined by the spectral function evaluated at the same ω. The regions of large joint DOS on this surface provides us with the dominate Fourier harmonics, and if these regions disperse, we see it in the FT of the LDOS. In Fig. 13 the QPI of the Abrikosov vortex is provided for cuts in k-space along the nodal direction, and it indicates we have dispersing quasiparticles by the change in Fourier harmonics.

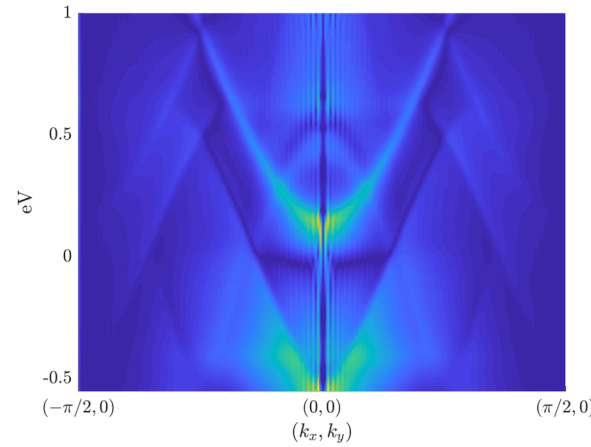

FIG. 13. The Fourier transform of the LDOS for an Abrikosov vortex of the PDW state for a range of probing voltages. We take cuts along the line $k_y = 0$ and plot the absolute value of the FT vs probing voltage. This figure showcases the QPI for the Abrikosov vortex, for which we note the dispersing quasiparticles; hence, these patterns do not represent a bound state. We suppressed the intensity around the Γ-point in this plot. A similar pattern of the QPI is present in the case of the double dislocation, suggesting it too does not possess bound quasiparticles.

APPENDIX E: TUNNELING DOS COMPARISON

Here we compare the plots corresponding to the tunneling DOS for the half-vortex outside the vortex core on its l.h.s. and r.h.s. [Figs. 14(a) and 14(b) respectively]. The tunneling DOS are labeled with only x coordinates to indicate how far we are in respect to the half-vortex core (x being measured relative to its center). This indicates we are looking at consecutive x positions in a given subfigures as well as we are comparing curves to the left (negative sign) and right

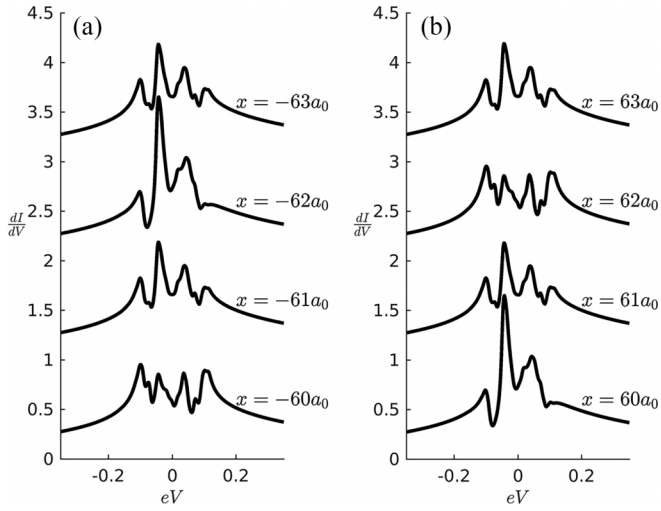

FIG. 14. Comparison of $\frac{dI}{dV}$ curves related to the tunneling DOS for the half-vortex (taken to live on the CuO bonds and not the center of the plaquette) at different lattice sites, indicated with the x position relative to the vortex core (with a relative shift of 1 between curves). We look at two sets of curves taken outside the vortex core of radius $r_0 = 24a_0$, (a) one to the left (negative x) and (b) one to the right (positive x). Both sets of curves repeat every four lattice spacings (in x), like an LO state. This indicates a relative shift between the curves in the two columns by two lattice spacings. The shift seen in these plots are a result of the jump in θ_+, defined in Eq. (2.8), occurring across the core of the vortex. (positive sign) of the vortex. The particular positions used for the representative curves are somewhat arbitrary in the sense we want only positions outside the core. Also, note that the defect is placed on the CuO bonds here opposed to the center of the plaquette as was done in the main text for the LDOS. The spectral functions corresponding to these two situations are equivalent, meaning the energetics are very similar, but the shape of the dI/dV curves will certainly change character since the gap amplitude takes on different values on the lattice sites.

Both sets of curves, to the right and to the left of the vortex core, have a periodicity of four lattice spacings, just like that of the pure PDW in the text (the same conclusion holds for the placement of the defect at the center of the plaquette). However, unlike a pure LO state the data appear to have a relative shift of two lattice spacings when comparing the curves from the right to the left (again this holds true for the half-vortex placed at the center of the plaquette). As was discussed in the text, this is due to the jump in θ_+ by $\pi/2$ across the half-vortex's core and can be explained as an accumulation in phase due to the nonzero COM momentum of our Cooper pairs; that is, $\mathbf{Q} \cdot \mathbf{r} = \pi/2$ if $\mathbf{r} = 2a_0\mathbf{e}_x$. This is a smoking gun signature of the half-vortex since a bona-fide LO state would not break inversion symmetry like so.

Now we compare the tunneling DOS of our topological defects inside and outside the core of the vortex [Figs. 15(a) and 15(b), respectively]. The Abrikosov vortex and the double dislocation both resemble a free particle tunneling DOS, albeit some additional wiggles. This is simply because we are not

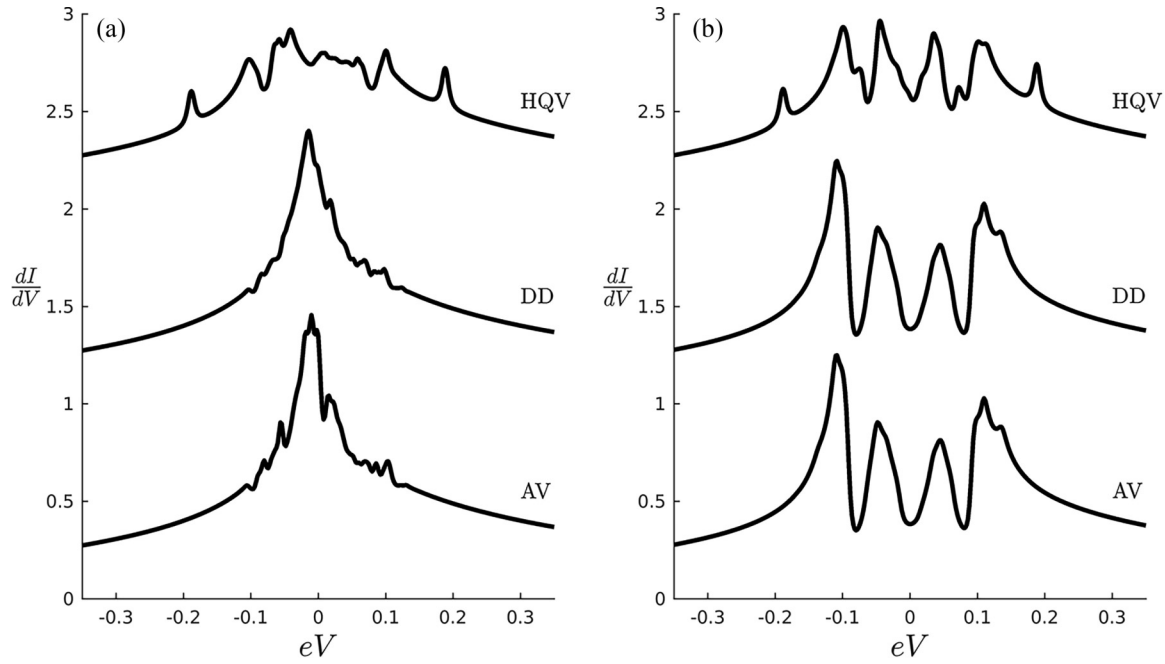

FIG. 15. Comparison of $\frac{dI}{dV}$ curves related to the tunneling DOS for the half-vortex, the double dislocation, and the Abrikosov vortex at two different lattice sites. The amplitudes are expressed in arbitrary units, each being normalized to the scale of the respective defect. In terms of fractions of the halo radius, $r_0 = 24a_0$, the plots are taken at a distance of (a) $0.025r_0$ and (b) $4r_0$ in respect to the vortex cores. Inside the core (a), the double dislocation and the Abrikosov vortex resemble a free particle dispersion since both the PDW components are small here. However, in the case of the half-vortex the core state is still superconducting, resembling a squeezed in FF state. Outside the core (b) all the curves resemble the pure PDW, but the half-vortex possesses additional satellite peaks due to the fact it possesses inequivalent PDW components.

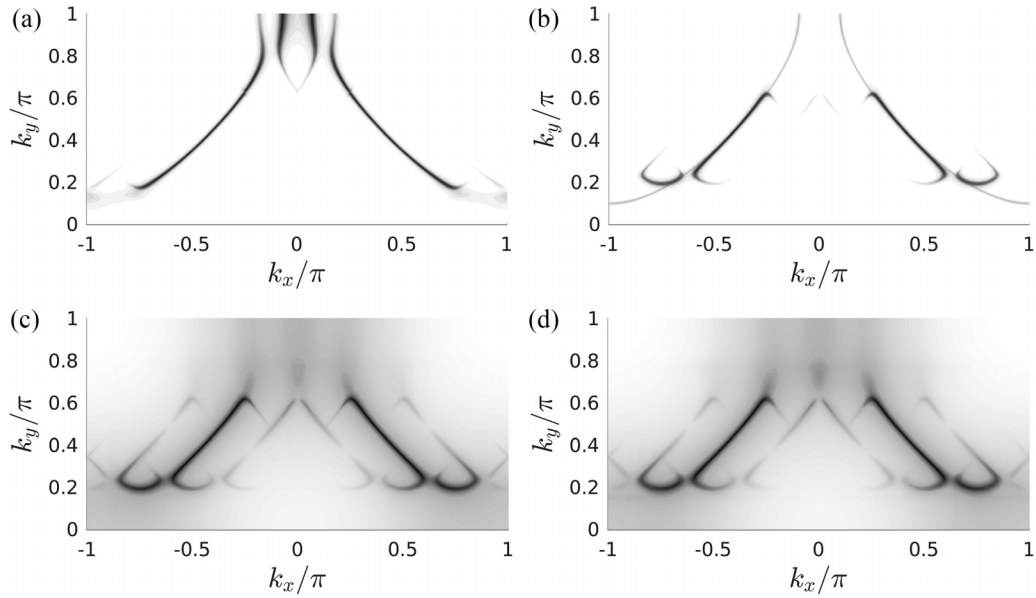

FIG. 16. Comparison plots of various Fermi surfaces. First, we provide a plot for (a) a defect-free PDW with an s-wave form factor compared with (b) a defect-free PDW with a d-wave form factor superimposed with the normal state dispersion (shown in light gray). The main arcs seen in both plots correspond to the normal state dispersion. In (c) we have a log plot of the Abrikosov vortex with a d-wave form factor, which greatly resembles the double dislocation and the pure PDW. Both defects prompt a slight redistribution of spectral weight, but nothing too dramatic like the half-vortex. Weaker features are uncovered with the log plots where the additional arcs correspond to the normal state dispersion shifted by $\pm\mathbf{Q}$.

right at the center of the core. Also, notice that the curves for these two defects are not in perfect agreement here, due to the form of the topological defect. Indeed, the electron DOS has to be distinct in the core of each vortex due to the difference in the respective defect. The half-vortex still possesses signatures of superconductivity in the core due to the fact it has FF character there. In fact, it resembles a squeezed in FF state.

Outside the core the double dislocation and the Abrikosov vortex look almost identical to one another and also the pure PDW (LO state). This is because the topological defect has less of an influence on the electronic states far away from the core. The half-vortex has additional wiggles in its tunneling DOS corresponding to satellite peaks. These additional peaks arise here and not for the other two defects because of the half-vortex's inequivalent Fourier components.

APPENDIX F: COMPARISON OF SPECTRAL FUNCTIONS FOR s-WAVE AND d-WAVE FORM FACTORS AND ADDITIONAL ORDER PARAMETERS

In this Appendix we compare some additional spectral functions not included in the main text. First, let's focus on the spectral functions corresponding to defect-free PDW states, one with an s-wave form factor and the other d-wave [Figs. 16(a) and 16(b), respectively]. The normal state dispersion is retained in both cases along the so-called Fermi arcs, so certain features are robust. The LDOS looks more or less the same for both form factors (not shown). Figure 16(c) is the natural log of the spectral function corresponding to the Abrikosov vortex, which closely resembles the double dislocation (not shown). Slight redistributions of the spectral weights occur for both these defects, but nothing as dramatic as that seen in the case of the half-vortex.

[1] E. Fradkin, S. A. Kivelson, and J. M. Tranquada, Colloquium: Theory of intertwined orders in high temperature superconductors, Rev. Mod. Phys. **87**, 457 (2015).

[2] D. F. Agterberg, J. S. Davis, S. D. Edkins, E. Fradkin, D. J. V. Harlingen, S. A. Kivelson, P. A. Lee, L. Radzihovsky, J. M. Tranquada, and Y. Wang, The physics of pair-density waves: Cuprate superconductors and beyond, Annu. Rev. Condens. Matter Phys. **11**, 231 (2020).

[3] M. Hücker, M. v. Zimmermann, G. D. Gu, Z. J. Xu, J. S. Wen, G. Xu, H. J. Kang, A. Zheludev, and J. M. Tranquada, Stripe order in superconducting $La_{2-x}Ba_xCuO_4$ ($0.095 < x < 0.155$), Phys. Rev. B **83**, 104506 (2011).

[4] Q. Li, M. Hücker, G. D. Gu, A. M. Tsvelik, and J. M. Tranquada, Two-dimensional superconducting fluctuations in stripe-ordered $La_{1.875}Ba_{0.125}CuO_4$, Phys. Rev. Lett. **99**, 067001 (2007).

[5] R. Zhong, J. A. Schneeloch, H. Chi, Q. Li, G. Gu, and J. M. Tranquada, Evidence for magnetic-field-induced decoupling of superconducting bilayers in $La_{2-x}Ca_{1+x}Cu_2O_6$, Phys. Rev. B **97**, 134520 (2018).

[6] A. A. Schafgans, A. D. LaForge, S. V. Dordevic, M. M. Qazilbash, W. J. Padilla, K. S. Burch, Z. Q. Li, S. Komiya, Y. Ando, and D. N. Basov, Towards two-dimensional superconductivity in $La_{2-x}Sr_xCuO_4$ in a moderate magnetic field, Phys. Rev. Lett. **104**, 157002 (2010).

[7] B. Lake, H. M. Rønnow, N. B. Christensen, G. Aeppli, K. Lefmann, D. F. McMorrow, P. Vorderwisch, P. Smeibidl, N. Mangkorntong, T. Sasagawa, M. Nohara, H. Takagi, and T. E. Mason, Antiferromagnetic order induced by an applied magnetic field in a high temperature superconductor, Nature (London) **415**, 299 (2002).

[8] P. M. Lozano, G. D. Gu, J. M. Tranquada, and Q. Li, Experimental evidence that zinc impurities pin pair-density-wave order in $La_{2-x}Ba_xCuO_4$, Phys. Rev. B **103**, L020502 (2021).

[9] H. Huang, S.-J. Lee, Y. Ikeda, T. Taniguchi, M. Takahama, C.-C. Kao, M. Fujita, and J.-S. Lee, Two-dimensional superconducting fluctuations associated with charge-density-wave stripes in $La_{1.87}Sr_{0.13}Cu_{0.99}Fe_{0.01}O_4$, Phys. Rev. Lett. **126**, 167001 (2021).

[10] E. Berg, E. Fradkin, E.-A. Kim, S. A. Kivelson, V. Oganesyan, J. M. Tranquada, and S. C. Zhang, Dynamical layer decoupling in a stripe-ordered high-T_c superconductor, Phys. Rev. Lett. **99**, 127003 (2007).

[11] J. D. Axe, A. H. Moudden, D. Hohlwein, D. E. Cox, K. M. Mohanty, A. R. Moodenbaugh, and Y. Xu, Structural phase transformations and superconductivity in $La_{2-x}Ba_xCuO_4$, Phys. Rev. Lett. **62**, 2751 (1989).

[12] J. D. Axe and M. Crawford, Structural instabilities in lanthanum cuprate superconductors, J. Low Temp. Phys. **95**, 271 (1994).

[13] K. Fujita, A. R.Schmidt, E.-A. Kim, M. J. Lawler, D. H. Lee, J. C. Davis, H. Eisaki, and S. Uchida, Spectroscopic imaging STM studies of electronic structure in the superconducting and pseudogap phases of cuprate high-T_c superconductors, J. Phys. Soc. Jpn. **81**, 011005 (2012).

[14] Z. Du, H. Li, S. H. Joo, E. P. Donoway, J. Lee, J. S. Davis, G. Gu, P. D. Johnson, and K. Fujita, Imaging the energy gap modulation of the cuprate pair-density-wave state, Nature (London) **580**, 65 (2020).

[15] S. D. Edkins, A. Kostin, K. Fujita, A. P. Mackenzie, H. Eisaki, S. Uchida, M. J. Lawler, E.-A. Kim, J. Davis, and M. H. Hamidian, Magnetic-field induced pair density wave in the cuprate vortex halo, Science **364**, 976 (2019).

[16] Y. Wang, S. D. Edkins, M. H. Hamidian, J. C. Seamus Davis, E. Fradkin, and S. A. Kivelson, Pair density waves in superconducting vortex halos, Phys. Rev. B **97**, 174510 (2018).

[17] A. Aishwarya, J. May-Mann, A. Raghavan, L. Nie, M. Romanelli, S. Ran, S. R. Saha, J. Paglione, N. P. Butch, E. Fradkin, and V. Madhavan, Magnetic-field-sensitive charge density waves in the superconductor UTe_2, Nature (London) **618**, 928 (2023).

[18] Q. Gu, J. P. Carroll, S. Wang, S. Ran, C. Broyles, H. Siddiquee, N. P. Butch, S. R. Saha, J. Paglione, J. C. S. Davis, and X. Liu, Detection of a pair density wave state in UTe_2, Nature (London) **618**, 921 (2023).

[19] Y. Liu, T. Wei, G. He, Y. Zhang, Z. Wang, and J. Wang, Pair density wave state in a monolayer high-T_c iron-based superconductor, Nature (London) **618**, 934 (2023).

[20] H. Zhao, R. Blackwell, M. Thinel, T. Handa, S. Ishida, X. Zhu, A. Iyo, H. Eisaki, A. N. Pasupathy, and K. Fujita, Smectic pair-density-wave order in $EuRbFe_4As_4$, Nature (London) **618**, 940 (2023).

[21] H. Zhao, H. Li, B. R. Ortiz, S. M. L. Teicher, T. Park, M. Ye, Z. Wang, L. Balents, S. D. Wilson, and I. Zeljkovic, Cascade of correlated electron states in the kagome superconductor csv_3sb_5, Nature (London) **599**, 216 (2021).

[22] H. Chen, H. Yang, B. Hu, Z. Zhao, J. Yuan, Y. Xing, G. Qian, Z. Huang, G. Li, Y. Ye, S. Ma, S. Ni, H. Zhang, Q. Yin, C. Gong, Z. Tu, H. Lei, H. Tan, S. Zhou, C. Shen *et al.*, Roton pair density wave in a strong-coupling kagome superconductor, Nature (London) **599**, 222 (2021).

[23] A. I. Larkin and Y. N. Ovchinnikov, Inhomogeneous state of superconductors, Sov. Phys. JETP **20**, 762 (1965) [J. Exper. Theor. Phys. (U.S.S.R.) **47**, 1136 (1964)].

[24] P. Fulde and R. A. Ferrell, Superconductivity in a strong spin-exchange field, Phys. Rev. **135**, A550 (1964).

[25] E. Berg, E. Fradkin, S. A. Kivelson, and J. M. Tranquada, Striped superconductors: How spin, charge and superconducting orders intertwine in the cuprates, New J. Phys. **11**, 115004 (2009).

[26] E. Berg, E. Fradkin, and S. A. Kivelson, Theory of the striped superconductor, Phys. Rev. B **79**, 064515 (2009).

[27] P. A. Lee, Amperean pairing and the pseudogap phase of cuprate superconductors, Phys. Rev. X **4**, 031017 (2014).

[28] J. Bardeen, L. N. Cooper, and J. R. Schrieffer, Theory of superconductivity, Phys. Rev. **108**, 1175 (1957).

[29] J. R. Schrieffer, *Theory of Superconductivity* (Addison-Wesley, Redwood City, CA, 1964).

[30] F. Loder, A. P. Kampf, and T. Kopp, Superconducting state with a finite-momentum pairing mechanism in zero external magnetic field, Phys. Rev. B **81**, 020511(R) (2010).

[31] F. Loder, S. Graser, M. Schmid, A. P. Kampf, and T. Kopp, Modeling of superconducting stripe phases in high-T_c cuprates, New J. Phys. **13**, 113037 (2011).

[32] J. Wårdh and M. Granath, Effective model for a supercurrent in a pair-density wave, Phys. Rev. B **96**, 224503 (2017).

[33] J. Wårdh, B. M. Andersen, and M. Granath, Suppression of superfluid stiffness near a Lifshitz-point instability to finite-momentum superconductivity, Phys. Rev. B **98**, 224501 (2018).

[34] A. Himeda, T. Kato, and M. Ogata, Stripe states with spatially oscillating d-wave superconductivity in the two-dimensional $t-t'-J$ model, Phys. Rev. Lett. **88**, 117001 (2002).

[35] P. Corboz, T. M. Rice, and M. Troyer, Competing states in the t-J model: Uniform d-wave state versus stripe state, Phys. Rev. Lett. **113**, 046402 (2014).

[36] B. Ponsioen, S. S. Chung, and P. Corboz, Superconducting stripes in the hole-doped three-band Hubbard model, Phys. Rev. B **108**, 205154 (2023).

[37] K. S. Huang, Z. Han, S. A. Kivelson, and H. Yao, Pair-density-wave in the strong coupling limit of the Holstein-Hubbard model, npj Quantum Mater. **7**, 17 (2022).

[38] H.-C. Jiang, Pair density wave in the doped three-band Hubbard model on two-leg square cylinders, Phys. Rev. B **107**, 214504 (2023).

[39] R. Soto-Garrido, G. Y. Cho, and E. Fradkin, Quasi-one-dimensional pair density wave superconducting state, Phys. Rev. B **91**, 195102 (2015).

[40] R. Soto-Garrido and E. Fradkin, Pair-density-wave superconducting states and electronic liquid-crystal phases, Phys. Rev. B **89**, 165126 (2014).

[41] D. Shaffer, F. J. Burnell, and R. M. Fernandes, Weak-coupling theory of pair density wave instabilities in transition metal dichalcogenides, Phys. Rev. B **107**, 224516 (2023).

[42] E. Berg, E. Fradkin, and S. A. Kivelson, Pair-density-wave correlations in the Kondo-Heisenberg model, Phys. Rev. Lett. **105**, 146403 (2010).

[43] A. Jaefari and E. Fradkin, Pair-density-wave superconducting order in two-leg ladders, Phys. Rev. B **85**, 035104 (2012).

[44] E. Berg, E. Fradkin, and S. A. Kivelson, Charge 4*e* superconductivity from pair density wave order in certain high temperature superconductors, Nat. Phys. **5**, 830 (2009).

[45] D. F. Agterberg and H. Tsunetsugu, Dislocations and vortices in pair-density-wave superconductors, Nat. Phys. **4**, 639 (2008).

[46] S. Baruch and D. Orgad, Spectral signatures of modulated *d*-wave superconducting phases, Phys. Rev. B **77**, 174502 (2008).

[47] P. M. R. Brydon, D. F. Agterberg, H. Menke, and C. Timm, Bogoliubov Fermi surfaces: General theory, magnetic order, and topology, Phys. Rev. B **98**, 224509 (2018).

[48] E. Berg, C.-C. Chen, and S. A. Kivelson, Stability of nodal quasiparticles in superconductors with coexisting orders, Phys. Rev. Lett. **100**, 027003 (2008).

[49] J. A. Robertson, S. A. Kivelson, E. Fradkin, A. C. Fang, and A. Kapitulnik, Distinguishing patterns of charge order; Stripes or checkerboards, Phys. Rev. B **74**, 134507 (2006).

[50] H. Miao, R. Fumagalli, M. Rossi, J. Lorenzana, G. Seibold, F. Yakhou-Harris, K. Kummer, N. B. Brookes, G. D. Gu, L. Braicovich, G. Ghiringhelli, and M. P. M. Dean, Formation of incommensurate charge density waves in cuprates, Phys. Rev. X **9**, 031042 (2019).

[51] S. Lee, E. W. Huang, T. A. Johnson, X. Guo, A. A. Husain, M. Mitrano, K. Lu, A. V. Zakrzewski, G. A. de la Peña, Y. Peng, H. Huang, S.-J. Lee, H. Jang, J.-S. Lee, Y. I. Joe, W. B. Doriese, P. Szypryt, D. S. Swetz, S. Chi, A. A. Aczel *et al.*, Generic character of charge and spin density waves in superconducting cuprates, Proc. Natl. Acad. Sci. USA **119**, e2119429119 (2022).

[52] Ö. Fischer, M. Kugler, I. Maggio-Aprile, C. Berthod, and C. Renner, Scanning tunneling spectroscopy of high-temperature superconductors, Rev. Mod. Phys. **79**, 353 (2007).

[53] J. E. Hoffman, E. W. Hudson, K. M. Lang, V. Madhavan, H. Eisaki, S. Uchida, and J. Davis, A Four Unit Cell periodic pattern of quasi-particle states surrounding vortex cores in $Bi_2Sr_2CaCu_2O_{8+y}$, Science **295**, 466 (2002).

[54] C. Howald, H. Eisaki, N. Kaneko, and A. Kapitulnik, Coexistence of charged stripes and superconductivity in $Bi_2Sr_2CaCu_2O_{8+\delta}$, Proc. Natl. Acad. Sci. USA **100**, 9705 (2003).

[55] S. A. Kivelson, I. Bindloss, E. Fradkin, V. Oganesyan, J. Tranquada, A. Kapitulnik, and C. Howald, How to detect fluctuating stripes in high temperature superconductors, Rev. Mod. Phys. **75**, 1201 (2003).

[56] M. J. Lawler, K. Fujita, J. W. Lee, A. R. Schmidt, Y. Kohsaka, C. K. Kim, H. Eisaki, S. Uchida, J. C. Davis, J. P. Sethna, and E.-A. Kim, Electronic nematic ordering of the intra-unit-cell pseudogap states in underdoped $Bi_2Sr_2CaCu_2O_{8+\delta}$, Nature (London) **466**, 347 (2010).

[57] A. N. Pasupathy, A. Pushp, K. K. Gomes, C. V. Parker, J. Wen, Z. Xu, G. Gu, S. Ono, Y. Ando, and A. Yazdani, Electronic origin of the inhomogeneous pairing interaction in the high-tc superconductor $Bi_2Sr_2CaCu_2O_{8+\delta}$, Science **320**, 196 (2008).

[58] A. Mesaros, K. Fujita, S. D. Edkins, M. H. Hamidian, H. Eisaki, S.-i. Uchida, J. Davis, M. J. Lawler, and E.-A. Kim, Commensurate $4a_0$-period charge density modulations throughout the $Bi_2Sr_2CaCu_2O_{8+x}$ pseudogap regime, Proc. Natl. Acad. Sci. USA **113**, 12661 (2016).

[59] E. Babaev, Vortices with fractional flux in two-gap superconductors and in extended Faddeev model, Phys. Rev. Lett. **89**, 067001 (2002).

[60] R.-H. He, K. Tanaka, S.-K. Mo, T. Sasagawa, M. Fujita, T. Adachi, N. Mannella, K. Yamada, Y. Koike, Z. Hussain, and Z.-X. Shen, Energy gaps in the failed high-T_c superconductor $La_{1.875}Ba_{0.125}CuO_4$, Nat. Phys. **5**, 119 (2009).

[61] I. M. Vishik, W. S. Lee, R.-H. He, M. Hashimoto, Z. Hussain, T. P. Devereaux, and Z.-X. Shen, ARPES studies of cuprate Fermiology: Superconductivity, pseudogap and quasiparticle dynamics, New J. Phys. **12**, 105008 (2010).

[62] Here we take as the zero of energy the ground state value, E_G.

[63] D. F. Agterberg, M. Sigrist, and H. Tsunetsugu, Order parameter and vortices in the superconducting *Q*-phase of $CeCoIn_5$, Phys. Rev. Lett. **102**, 207004 (2009).

[64] Z. Dai, Y.-H. Zhang, T. Senthil, and P. A. Lee, Pair-density waves, charge-density waves, and vortices in high-T_c cuprates, Phys. Rev. B **97**, 174511 (2018).

[65] J. Meng, G. Liu, W. Zhang, L. Zhao, H. Liu, X. Jia, D. Mu, S. Liu, X. Dong, J. Zhang, W. Lu, G. Wang, Y. Zhou, Y. Zhu, X. Wang, Z. Xu, C. Chen, and X. J. Zhou, Coexistence of Fermi arcs and Fermi pockets in high temperature cuprate superconductors, Nature (London) **462**, 335 (2009).

[66] S. Chakravarty, C. Nayak, and S. Tewari, Angle-resolved photoemission spectra in the cuprates from the *d*-density wave theory, Phys. Rev. B **68**, 100504 (2003).

[67] A. Aishwarya, J. May-Mann, A. Almoalem, S. Ran, S. R. Saha, J. Paglione, N. P. Butch, E. Fradkin, and V. Madhavan, Melting of the charge density wave by generation of pairs of topological defects in UTe_2, Nat. Phys. **20**, 964 (2024).

[68] W. L. McMillan, Theory of discommensurations and the commensurate-incommensurate charge-density-wave phase transition, Phys. Rev. B **14**, 1496 (1976).

[69] J. M. Tranquada, $La_{2-x}Ba_xCuO_4$ as a superconducting Rosetta Stone, Physica C **614**, 1354371 (2023).

[70] Y. Imry and S.-k. Ma, Random-field instability of the ordered state of continuous symmetry, Phys. Rev. Lett. **35**, 1399 (1975).

[71] K. B. Efetov and A. I. Larkin, Charge-density wave in a random potential, Sov. Phys.–JETP **45**, 1236 (1977).

[72] D. F. Mross and T. Senthil, Spin- and pair-density-wave glasses, Phys. Rev. X **5**, 031008 (2015).

[73] E. Lieb, T. Schultz, and D. Mattis, Two soluble models of an antiferromagnetic chain, Ann. Phys. **16**, 407 (1961).